SIMULATION OF CONTAMINANT TRANSPORT IN GROUNDWATER SYSTEMS USING EULERIAN–LAGRANGIAN LOCALIZED ADJOINT METHODS

by

SIMON ZISMAN

B.S., Civil Engineering
Universidad Catolica Andres Bello
(1986)

Submitted in partial fulfillment
of the requirements
for the degree of

MASTER OF SCIENCE IN CIVIL ENGINEERING

at the

MASSACHUSETTS INSTITUTE OF TECHNOLOGY

February 1990

Signature of Author.....
Department Of Civil Engineering
November 6, 1989

Certified by.....
Michael A. Celia
Professor, Civil Engineering
Thesis Supervisor

Accepted by.....
Ole S. Madsen
Chairman, Departmental Committee on Graduate Students

To the memory of my grandfather,

Moises Zisman

SIMULATION OF CONTAMINANT TRANSPORT

IN GROUNDWATER SYSTEMS

USING EULERIAN–LAGRANGIAN LOCALIZED ADJOINT METHODS

by

Simon Zisman

Submitted to the Department of Civil Engineering
on November 6, 1989 in partial fulfillment of the
requirements for the degree of
Master of Science in Civil Engineering.

ABSTRACT

A numerical simulator is developed based on the the Eulerian–Lagrangian localized adjoint method (ELLAM) for the one–dimensional, constant–coefficient transient advective–diffusive–reactive equation. This equation describes the behavior of a dissolved contaminant in chemically and/or biologically reactive groundwater systems. The ELLAM was originally presented by Celia and co–workers (1989c) for the advective–diffusive equation.

This work provides further testing of the original ELLAM procedure and extends that development to include reactive transport. This extension involves the modification of weight or test functions, which appear in a weak form of the original governing equation, to reflect the influence of the reaction term. Numerical results demonstrate that the ELLAM procedure is mass conservative and that it properly accounts for both Dirichlet and Neumann boundary conditions, thus overcoming the two principal shortcomings of Eulerian–Lagrangian methods. In addition, results for the reactive case show that the presence of reactions may pose limits on the use of large Courant numbers which are possible in nonreactive transport.

Thesis Supervisor: Dr. Michael A. Celia

Title: Assistant Professor of Civil Engineering.

ACKNOWLEDGEMENTS

A number of people have given me their support, encouragement and constructive criticism during my stay at M.I.T. I have learned from them in many ways, professionally and personally, and I express gratitude to them all.

First, my sincerest and warmest thanks to my thesis advisor, Prof. Michael Celia, whose patient and tactful guidance and generous assistance have eased my way throughout the course of this project. Few individuals I know combine such keen insight, remarkable intelligence and human kindness. One could not ask for a better advisor.

Special thanks are extended to Professors Reinaldo Garcia, Manuel Vicente Mendez, Marco Falcon and Henry Power, at the Universidad Central de Venezuela, and to the faculty at the Parson's Laboratory of M.I.T., in the persons of Rafael Bras, Ignacio Rodriguez–Iturbe, Harry Hemond and Ole Madsen. Their dedication and intellectual standards have been an inspiration.

My fellow students and friends, Pavan Bakeri, Ede Ijjasz, Shuguang Li, J.J. Lee, Juan Manuel Pestana, Hari Rajaram, Andres Rodriguez and Tunu Savage, created an environment that was both stimulating to work in and a pleasure to live in. My thanks go to them.

Finally, a deep–hearted thank you to my parents, Elias and Adela, my brothers David and Ariel, my sister Adriana, and my grandmother Luisa. Their cheerful support and love has given me the strength to finish this work. Their contribution cannot be overstated.

CONTENTS

LIST OF FIGURES

LIST OF TABLES

Chapter 1: INTRODUCTION

1.1 Objectives

The primary motivation for the study of groundwater has traditionally been its importance as a resource. During recent years much of the emphasis in groundwater investigations has shifted from problems of groundwater supply to considerations of groundwater quality. It is nowadays generally recognized that both aspects of water resources – quantity and quality – are important and interdependent.

New uses of groundwater reservoirs such as *waste storage* and *artificial recharge* raise difficult questions about groundwater quality and its protection. A contaminated surface–water reservoir (e.g. river or lake) may be restored to health in a few years (or less) by the implementation of effective legislation for discontinuing contaminant emissions. In contrast, parts of a groundwater reservoir may be rendered useless for centuries by indiscriminate introduction of foreign, poor quality substances.

Hazardous substances have been found in many groundwater aquifers, indicating that waste disposal sites communicate with underground water reservoirs. This has prompted a growing number of studies of solute transport in groundwater systems.

Field observations, laboratory experiments and *mathematical models* provide means to understand and forecast the fate of subsurface contaminants. Once a mass transport problem has been properly formulated in mathematical terms, two methods of solution are possible in principle: (1) an analytic solution,

or (2) an approximate numerical solution.

Analytical solution techniques may be used for simple situations, or to obtain an initial estimation of contamination extent. For situations involving complex processes in heterogeneous and anisotropic formations under various initial and boundary conditions (e.g. multiple wells, multiple aquifers, aquifer–river interactions, etc.), it is necessary to resort to approximate numerical techniques.

This work focuses on a new numerical solution procedure, the Eulerian–Lagrangian localized adjoint method (ELLAM), recently developed by Celia and co–workers (1989c), and its application to the single species, one–dimensional constant–coefficient, transient advective–diffusive–reactive transport equation, which describes the behavior of a dissolved substance subject to both first– and zeroth–order reactions in a one–dimensional homogeneous saturated medium with steady–state flow.

The ELLAM consists of a space–time formulation based on Eulerian–Lagrangian techniques and the optimal test function (OTF) method (see Celia et al., 1989a, b). The Eulerian–Lagrangian localized adjoint method (ELLAM) development yields a conservative scheme and provides a systematic way to incorporate boundary conditions, thus overcoming two of the principal shortcomings of existing Eulerian–Lagrangian methods (see, for example, Neuman, 1981, 1984; Neuman and Sorek, 1982; Baptista et al., 1984).

The results of this work include, (1) examination of the behavior of the ELLAM in solving the advection–diffusion equation, and (2) extension of the ELLAM formulation to accommodate first–order reaction terms. Numerical examples demonstrate the influence of the reaction terms, as well as proper

treatment of boundary conditions.

1.2 Review of Relevant Literature

To make the essential ideas of the following discussion clear, consider the one–dimensional, constant–coefficient, transient advection–diffusion equation,

$$\frac{\partial c}{\partial t} + V \frac{\partial c}{\partial x} - D \frac{\partial^2 c}{\partial x^2} = 0$$

where c is the concentration of the dissolved substance [M/L^3], V is the fluid velocity [L/t], D is a diffusion coefficient [L^2/t], x is the space dimension [L] and t is the time dimension [t]. This equation can be written in *dimensionless* form by introducing the following variables,

$$\tau \equiv t/\Delta t, \qquad \xi \equiv x/\Delta x, \qquad C \equiv c/c_o$$

in which Δt and Δx are, respectively, typical time and space increments (usually taken as characteristic time and length scales of the phenomenon); C is the dimensionless concentration and c_o is a characteristic concentration. Thus, the original equation becomes,

$$\frac{\partial C}{\partial \tau} + Cu \frac{\partial C}{\partial \xi} - \rho \frac{\partial^2 C}{\partial \xi^2} = 0$$

where

$$Cu \equiv \frac{V\Delta t}{\Delta x}, \qquad \rho \equiv \frac{D\Delta t}{(\Delta x)^2}$$

Cu is the dimensionless (grid) Courant number, and ρ is referred to as a

dimensionless diffusivity.

The *nature* of the advection–diffusion equation can be conveniently characterized by the dimensionless (grid) *Peclet* number,

$$\mathrm{Pe} = \frac{\mathrm{Cu}}{\rho} = \frac{\mathrm{V}\Delta\mathrm{x}}{\mathrm{D}}$$

When Pe is small, diffusion dominates, and the equation behaves analogous to a model parabolic partial differential equation; when Pe is large, advection dominates, implying behavior analogous to first–order hyperbolic partial differential equations.

In non–uniform flow fields where the velocity is not constant, Pe may vary from point to point both in space and time. As a result of this variation, the advection–diffusion equation may vary in character within a given field and with time, being predominantly parabolic in some regions and predominantly hyperbolic in others. A numerical solution procedure for the advective–diffusive equation that neglects these contrasting behaviors will generally fail to produce meaningful results.

Numerical methods for solving the advection–diffusion equation can be classified into three major categories: (1) *Eulerian*, (2) *Lagrangian*, and (3) *Eulerian–Lagrangian.*

In the Eulerian viewpoint (or method), attention is focused on a definite domain, fixed in space. Independent variables are the coordinates of space and time. In the Lagrangian method the history of individual particles is described; that is, the position in space of any particle at any instant is given by the coordinates in some reference system, and these coordinates are functions of time –

the only independent variable of the process.

In the Eulerian method, the governing equation is discretized by means of a finite difference or finite element grid fixed in space. Eulerian techniques work well when diffusion is the dominant process (i.e. low Peclet numbers) and the concentration function is relatively smooth (no sharp fronts). However, when advection is the dominant process (high Pe) large concentration gradients may exist, giving rise to numerical difficulties (Pinder and Gray, 1977). In general, the solutions are characterized by (1) nonphysical oscillations in the vicinity of sharp fronts, resulting in overshoot (erroneously high values of concentration encountered as one approaches a sharp front from the upstream side), undershoot (analogous to overshoot but on the downstream side) and negative concentrations, and (2) numerical dissipation (causing the sharp front to be smeared).

One possible remedy to these numerical difficulties is the use of an extremely fine mesh. This option is in many situations impractical due to the excessive computational effort that it implies.

Alternative Eulerian approaches have been devised for advective dominated flows. These include classical upstream weighted finite differences (see, for example, Lapidus and Pinder, 1982) and a variety of finite element, or Petrov–Galerkin methods (Huyakorn, 1976; Heinrich et al., 1977; Hughes, 1978; Brooks and Hughes, 1982). The general idea of these methods is to account for the flow direction, resulting in an upstream bias (in the form of an arbitrary parameter) for the approximation. Limitations include: (1) introduction of artificial diffusion, and (2) the necessity of selecting an appropriate value for an arbitrary parameter that appears in the formulation.

More recently, Celia et al. (1989a, b) introduced a numerical solution procedure, referred to as the Optimal Test Function (OTF) method, in which – by using a weak form of the governing equation, together with weight (or test) functions that vary according to the degree of advection domination – no arbitrary parameter is employed.

Each of these methods (which are based exclusively on the Eulerian viewpoint) suffer from strict Courant number ($Cu \equiv V\Delta t/\Delta x$) limitations, which in the majority of cases must be less than one, and in some situations considerably less than one.

Due to the hyperbolic nature of advective transport, many researchers have considered *characteristic analysis* to complement the description of the phenomenon. Lagrangian methods, utilizing deforming grids or fixed grids in deforming coordinates have been developed (see, for example, Varoglu and Finn, 1980). In these formulations, the finite element equations become free of convective terms, resulting in a relatively well behaved diffusion–type problem.

Even though these Lagrangian methods are more powerful than existing Eulerian techniques (they are not plagued by Courant number limitations), they suffer from restrictions caused by grid displacements and deformations. Since subsurface environments are often characterized by highly nonuniform material properties, the movement of nodal points across material interfaces may cause difficulties in the handling of equation parameters, especially if sorption and chemical reactions are important. Such movement may also result in severe grid deformations, leading to numerical errors. When multiple sources exist, as in the case of chemical injection into the subsurface through several wells (artificial recharge), concentration fronts may propagate in opposite directions and cross

each other. This type of transport cannot be handled with the aid of deforming meshes or moving coordinates (Neuman, 1981).

The purpose of the Eulerian–Lagrangian methods (ELM's) is to combine the simplicity of the fixed Eulerian grid with the capability of the Lagrangian approach to treat the hyperbolic nature of advective transport. Eulerian–Lagrangian methods handle the advective component in a Lagrangian frame of reference (by using a characteristic tracking algorithm), and the diffusive component in a separate Eulerian (fixed) grid.

Neuman (1981, 1984), Neuman and Sorek (1982), and Baptista et al. (1984) introduced formulations in which advection is formally decoupled from diffusion. Since the advection and diffusion processes require different treatments, they are solved on separate space–time grids; results are then projected from one grid to the other by various piecewise interpolation procedures.

Although these versions produce results which are only slightly oscillatory and without numerical diffusion, they generally fail to conserve mass. In addition, the methods do not provide a general framework for incorporating boundary conditions.

The Eulerian–Lagrangian localized adjoint method (ELLAM) developed by Celia et al. (1989c) is a new numerical approach that incorporates concepts from the Optimal Test Functions (OTF) method and characteristic analysis to produce a space–time formulation which (1) employs no arbitrary parameters, (2) does not rely on any operator splitting or equation decomposition techniques, (3) produces approximations that possess the conservative property, and (4) provides a general framework that accommodates (in a systematic way) any form of boundary conditions.

1.3 Organization

The presentation of this work is organized into five chapters. Chapter 1 delineates the motivation, nature and scope of the research. Chapter 2 provides an overview of contaminant transport in groundwater systems. It focuses on the role of mathematical models as tools for understanding and forecasting solute transport in the subsurface. Topics covered include (1) sources of contamination, (2) groundwater models, (3) basic equations, (4) prediction models and (5) mass transport models. In Chapter 3 the salient features of the numerical solution procedure, the Eulerian–Lagrangian localized adjoint method (ELLAM), are detailed. The formulation for the advective–diffusive–reactive transport equation follows. Results of various test cases are presented in Chapter 4. These tests (which include the propagation of an initial step discontinuity, propagation of a Gauss hill, and solution of advective–diffusive–reactive problems) are intended to demonstrate the performance of the numerical method. Finally, Chapter 5 contains a general discussion of this work, including directions for future developments.

Chapter 2: CONTAMINANT TRANSPORT IN GROUNDWATER SYSTEMS

2.1 Introduction

This chapter provides an overview of contaminant transport in groundwater systems. The discussion concentrates on the role of mathematical models as tools for understanding and forecasting solute transport in subsurface systems. Topics covered include (1) sources of contamination, (2) groundwater models, (3) basic equations, (4) prediction models, and (5) mass transport models.

The term *groundwater* denotes all waters found beneath the ground surface. It includes water in the partially saturated layers above the water table and water contained in the zone of saturation. Numerous processes take place below the ground surface. Processes relevant to this work are those that deal with *mass transport*. In particular we are interested in the fate (i.e. spatial and temporal distribution) of contaminants that enter the groundwater system (the sources of contamination are discussed below). Once the mass transport problem is defined mathematically (usually by a set of coupled or uncoupled partial differential equations), numerical models can be employed to obtain a solution. The information provided by the model can be used, for example, to delineate adequate remediation measures.

2.2 Sources of Contamination

There are two main types of groundwater pollution caused by man: (1) pollution caused by the use of pesticides, herbicides, and fertilizers over agricultural lands, where the source of contamination covers a *relatively large*

area, and (2) pollution caused by industries and municipalities, which is generally more *localized.*

Some of the *localized* sources (which are related to activities such as mining, nuclear power development, disposal of refuse, sewage, industrial wastes, etc.) that contribute contaminants to the groundwater zone (U.S. Environmental Protection Agency, 1977) include: (1) industrial wastewater impoundments, (2) land disposal sites for solid wastes, (3) well disposal of liquid wastes, (4) septic tanks and cesspools, (5) collection, treatment, and disposal plants for municipal wastewater, (6) land spreading of sludges, (7) brine disposal from petroleum exploration and development, (8) disposal of mine wastes, (9) disposal of radioactive wastes, (10) chemical spills, (11) leaks from underground storage facilities, etc.

Industrial wastewater impoundments are natural or artificial depressions in the ground used for the temporary or permanent storage and/or disposal of liquid wastes. Many of the industrial impoundments have no impermeable liner. Therefore, the hazardous waste can easily infiltrate downward toward underlying groundwaters.

Solid waste land disposal occurs as a result of several types of operations: dumps, landfills, sanitary landfills, and secured landfills. A *dump* is an uncovered disposal site where solid or liquid wastes are deposited. If the wastes are periodically covered with natural soils, a *landfill* is created. *Sanitary landfills* are sites were solid wastes are disposed of by compacting the waste and covering it at the end of each operating day to minimize environmental hazards. If efforts are made to prohibit contaminant movement between the waste and the surrounding environment (particularly the groundwater), it is called a *secured landfill.*

Secured landfills are generally designed to accept highly toxic waste and are supposed to be continuously monitored.

The mechanism of groundwater contamination by solid waste land disposal facilities is mainly through the generation of *leachate*, with subsequent downward movement to underlying groundwaters. Leachate generation is due in part to the precipitation which percolates through the solid waste, dissolves soluble components, and carries them out of the waste. This liquid, together with any liquid waste placed in the fill and other liquids coming from waste decomposition, constitute the leachate.

Injection of liquid wastes into subsurface strata (waste disposal through wells or artificial recharge) has been widely adopted as a waste disposal practice (Javandel et al., 1984). In general, two types of wells are used: (1) shallow wells, and (2) deep wells. Storm water, spent cooling water, and sewage effluent are generally injected through relatively shallow wells. Sometimes these wells are completed in the unsaturated zone; however, they often penetrate the saturated zone and thus lead the recharging liquid directly into the groundwater.

Large volumes of brine produced by petroleum industries, geothermal energy production, and other sources are generally injected through deep wells (ranging in depth between approximately 300 to 2000 m) into saline water aquifers. Hazardous chemicals, petrochemicals, and pharmaceuticals are also injected.

It was formerly believed that, due to adsorption and biodegradation, injected wastewater became free of contamination after passing a short distance through the porous medium. Recently, however, it has been shown that some of the organic chemicals and viruses can migrate long distances through aquifers

before being (if at all) neutralized.

2.3 Groundwater Models

A groundwater model can be defined as a simplified version of a real groundwater system, describing the features essential to the purpose for which the model was developed, and including various assumptions and constrains pertinent to the system. They can be classified as (1) *prediction models*, used to forecast changes in the state of the system (e.g. position of the water table, concentration of a contaminant, etc.), (2) *resource management models*, developed to aid planning by delimiting courses of action that satisfy stated management objectives (e.g. location of wells, pumping rates, etc.) and constraints (e.g. maximum pumping rates, drawdowns, etc.), and (3) *identification models*, which determine system parameters such as porosity, permeability, etc. that serve as input data for both of the models above.

Most groundwater models are designed to solve a partial differential equation or a set of partial differential equations such as the equations of groundwater flow and transport. These equations will be discussed in the following section.

2.4 Basic Equations

In groundwater modeling we are concerned with the fluids contained in the aquifer system. Such fluid is generally described by stating: (1) the pressure of the fluid (which in certain simplifying instances, e.g. constant density, can be substituted for the hydraulic head or piezometric head), (2) the composition of

the fluid, and (3) the energy contained in the fluid. In the general case, three *coupled* partial differential equations (PDE's) are utilized to describe the fluid; these are (Van der Heijde et al., 1985): (1) a PDE for pressure (i.e., a statement of conservation of mass and momentum, the latter in the form of Darcy's law), which is commonly referred to as the *flow equation*:

$$\frac{\partial}{\partial t}(\rho n) - \nabla\cdot\frac{\rho \mathbf{k}}{\mu}(\nabla P - \rho \mathbf{g}) = q$$

(2) a partial differential equation for composition; in the case where more than one chemical constituent (species) of the fluid is of interest, this becomes a set of partial differential equations:

$$\frac{\partial}{\partial t}(\rho n w) - \nabla\cdot[\ \rho w\frac{\mathbf{k}}{\mu}(\nabla P - \rho \mathbf{g})\ ] - \nabla\cdot(\rho D)\cdot\nabla w = -qw$$

and (3) a partial differential equation for the internal energy of the fluid, generally either the temperature or the enthalpy of the fluid:

$$\frac{\partial}{\partial t}[n\rho U + (1-n)(\rho C_p)_R T] - \nabla\cdot[\ (\rho \mathbf{k}/\mu)\ H\ (\nabla P - \rho \mathbf{g})\ ] - \nabla\cdot K\cdot\nabla T = -q_L - qC_pT$$

where

C concentration [M/L^3], equal to ρw;

C_p specific heat [$Cal/M\cdot T$];

D hydrodynamic dispersion tensor [L^2/t];

g gravitational acceleration vector (directed downward) [L/t^2];

H enthalpy [Energy];

k intrinsic hydraulic conductivity tensor [L^2];

K thermal conductivity tensor of the aquifer [Cal/L·t·T];

n porosity [L^3/L^3];

P pressure [$M/L \cdot t^2$];

q mass rate of production or injection of liquid [$M/L^3 \cdot t$];

q_L rate of heat loss [Heat/$L^3 \cdot t$];

R rock phase;

t time [t];

T temperature [T];

U internal energy [Energy];

w mass fraction [M/M];

ρ density [M/L^3];

μ dynamic viscosity [$M/L \cdot t$];

In many instances the coupling may be negligible, and the equations can be treated as uncoupled and solved separately. For example, when the change in temperature is unimportant, the system can be considered as isothermal, eliminating consideration of temperature or enthalpy.

In order to solve the partial differential equation, or set of partial differential equations, for groundwater systems, the following elements must be completely described: (1) the distribution of the parameters through the space of interest (e.g. porosity, permeability, compressibility of both the fluid and the medium – which are commonly combined mathematically into a single parameter, the "specific storage", or in the case of unconfined systems, the "specific yield" –, etc.), (2) initial conditions for pressure, composition, and temperature or enthalpy, (3) the sources and sinks of interest and their variation

with time, and (4) the boundary conditions at the margins of the space of interest.

2.5 Prediction Models

Prediction models serve the purpose of forecasting system responses (e.g. pressure of the fluid, concentration of a substance, etc.) given system parameters and adequate initial and boundary conditions. In general they foretell the state of a single phase or multiphase system; one phase of which is usually moving groundwater. Other fluid phases comprising the system may be either mobile or immobile; the terms single phase or multiphase pertain to the mobile phases only. A fluid phase is referred to as homogeneous if its density and viscosity are uniform in space; otherwise it is nonhomogeneous.

Prediction models may be subdivided into three major categories: (1) flow, (2) heat transport and (3) mass transport.

Flow models determine quantitative aspects of groundwater flow such as direction and rate of flow, changes in water level, interference effects of wells, etc.

Heat transport models couple the flow of heat with water or steam for problems where thermal effects are important (e.g. problems associated with hot springs, geothermal reservoirs, and heat storage).

Mass transport models deal primarily with questions of groundwater quality. They are used to predict the movement and concentration of various pollutants such as radionuclides, leached contaminants from landfills, salt water intruding in coastal areas, etc.

2.6 Mass Transport Models

Mass transport models are more complex than flow models in that they consider quality in conjunction with quantity. In principle, a mass transport model contains a flow submodel which computes the fluid velocity and then utilizes these velocities in a quality submodel which transports the contaminants in the flow field.

The physical processes that control the movement of contaminants in subsurface systems depend on the nature of the substance: (1) miscible substances (i.e. those that are completely soluble in water) migrate by means of *advection*, *hydrodynamic dispersion* and *molecular diffusion*; in contrast, (2) immiscible substances (e.g. oily substances that exist in a liquid state in contact with water in a manner that does not lead to mixing of the oils in a dissolved form) are transported by advection alone. Loss or gain of solute mass can occur as a result of chemical or biochemical reactions or radioactive decay.

Under certain circumstances (e.g. low concentrations of contaminants) flow and quality submodels can operate independently. In other cases, however, their mutual effects cannot be uncoupled. Thus relatively high contaminant concentrations affect the flow pattern (i.e. fluid velocity) of the groundwater, which in turn affects the movement and spreading of the contaminants; this requires interactive coupling between the flow and quality submodels.

Transport processes are termed nonconservative if transformations by reactions and phase change are involved; otherwise the processes are conservative.

The myriad of chemical and biochemical reactions that can alter

contaminant concentrations in groundwater systems can be grouped in six categories (Freeze and Cherry, 1979): (1) adsorption–desorption reactions, (2) acid–base reactions, (3) solution–precipitation reactions, (4) oxidation–reduction reactions, (5) ion pairing or complexation, and (6) microbial cell synthesis. Radioactive contaminants are influenced by radioactive decay in addition to the nonradiogenic processes.

Chapter 3: NUMERICAL DEVELOPMENT

3.1 Introduction

The Eulerian–Lagrangian localized adjoint method (ELLAM) is a new numerical solution procedure developed by Celia and co–workers (1989c) for the one–dimensional, transient advective–diffusive transport equation. This method consists of a space–time formulation that combines notions from (1) characteristic analysis and (2) the Optimal Test Function (OTF) method (see Celia et al., 1989a, b).

In this chapter the original ELLAM procedure is extended and applied to the one–dimensional, constant coefficient, transient advective–diffusive–reactive transport equation. The extension involves the modification of test functions, which appear in a weak form of the original governing equation, to reflect the influence of the reaction term.

To set the stage for the following discussion, consider the model one–dimensional transient reactive transport equation $\mathscr{L}u(x,t) = f(x,t)$ defined over some rectangular space–time domain $\Omega_{x,t}$. $\mathscr{L}$ denotes the governing differential operator, f(x,t) a known forcing function and u(x,t) the dependent variable of interest. Let the spatial domain Ω_x be divided into E intervals separated by E + 1 node points $\{ x_0, x_1, ..., x_E \}$ and the temporal domain Ω_t discretized into time steps $\{ t^0, t^1, ..., t^n, t^{n+1}, ... \}$.

The numerical development begins by considering a *weak form* of the governing differential equation. The weak form is obtained by multiplying the original equation by a set of linearly independent weight or test functions,

$\{ w_0(x,t), w_1(x,t), ..., w_E(x,t) \}$, and integrating the resulting expression over the domain $\Omega_{x,t}$.

A fundamental difference between the Eulerian–Lagrangian localized adjoint method and standard finite elements or Petrov–Galerkin methods is that, in the ELLAM, the functional form of weight or test functions $\{ w_i(x,t) \}_{i=0}^{E}$ is unknown a priori. Moreover, this functional form depends on the governing differential equation being considered (see the discussion on localized adjoint methods in paragraph 3.2). This means that different governing equations will require, in general, different definitions for test functions.

The way to determine the functional form of test functions is the following. Assuming that the solution $u(x,t)$ and the test functions $w_i(x,t)$ are sufficiently smooth (i.e. all integrals involved are well–defined), the weak form of the original differential equation integrating over $\Omega_{x,t}$ is replaced by a sum of elemental integrals that have the same integrand but are integrated over space–time subregions or elements Ω_e, $e = 1, 2, ..., E$. Next, integration by parts is (repeatedly) applied to the *localized elemental integrals* in order to obtain an integrand that contains the adjoint operator of $\mathscr{L}$ acting on w_i, that is, $\mathscr{L}^* w_i(x,t)$. Once this is accomplished, *each* elemental integral becomes equal to the sum of (1) line integrals along the *boundary* of the element, and (2) an integral over the *interior* of the element which contains the expression $\mathscr{L}^* w_i(x,t)$.

Now, if $\mathscr{L}^* w_i(x,t)$ is forced to be zero within the interior of each element Ω_e, all interior element integrations can be eliminated and the weak form of the original differential equation integrated over $\Omega_{x,t}$ can be replaced by a sum of elemental boundary integrals. Furthermore, a functional form of $w_i(x,t)$ can be

derived from $\mathcal{L}^* w_i(x,t) = 0$.

The expression $\mathcal{L}^* w_i(x,t) = 0$ is referred to as the *homogeneous adjoint equation*; it involves only the test functions and their derivatives. The solution of the homogeneous adjoint equation is the required functional form of the test functions. When the governing equation, $\mathcal{L} u(x,t) = f(x,t)$, is a partial differential equation (PDE), the homogeneous adjoint equation is itself a PDE with an infinite number of possible solutions. One must be careful to choose an appropriate functional form from the numerous available. Different forms will produce, in general, different algebraic approximations.

In summary, the first step of the numerical procedure is to choose a set of test functions so that each function satisfies the homogeneous adjoint equation within each subregion Ω_e. Next, the weak form of the original differential equation, integrated over $\Omega_{x,t}$, is replaced by a sum of elemental boundary integrals. Subsequent evaluation of these remaining terms leads to the algebraic approximation of interest.

The basis for the name "... localized adjoint method" is that the homogeneous adjoint equation $\mathcal{L}^* w_i(x,t) = 0$ is satisfied for each $w_i(x,t)$ only within specified (or localized) subregions of the domain $\Omega_{x,t}$.

3.2 Localized Adjoint Methods (LAM's)

Consider the following partial differential equation (PDE) in space–time,

$$\mathcal{L}u(\underset{\sim}{x}) = f(\underset{\sim}{x}), \quad \underset{\sim}{x} \in \Omega \tag{3.1}$$

where $\mathcal{L}$ is a differential space–time operator, $u(\underset{\sim}{x})$ is the dependent variable of interest, and $\underset{\sim}{x}$ is the vector of independent variables. The weak form of (3.1) is given by

$$\int_{\Omega} [\ \mathcal{L}u(\underset{\sim}{x})\ ]\ w_i(\underset{\sim}{x})\ d\underset{\sim}{x} = \int_{\Omega} f(\underset{\sim}{x})\ w_i(\underset{\sim}{x})\ d\underset{\sim}{x} \tag{3.2}$$

where $w_i(\underset{\sim}{x})$ is a weight or test function. Assuming that $u(\underset{\sim}{x})$ and $w_i(\underset{\sim}{x})$ are sufficiently smooth, then the integral on the left side of (3.2) can be written equivalently as

$$\int_{\Omega} [\ \mathcal{L}u(\underset{\sim}{x})\ ]\ w_i(\underset{\sim}{x})\ d\underset{\sim}{x} = \sum_{e} \int_{\Omega_e} [\ \mathcal{L}u(\underset{\sim}{x})\ ]\ w_i(\underset{\sim}{x})\ d\underset{\sim}{x} \tag{3.3}$$

where Ω_e is an element subdomain such that

$$\bigcup_{e} \Omega_e = \Omega, \quad \bigcap_{e} \Omega_e = \emptyset \tag{3.4}$$

Now, let integration by parts be (repeatedly) applied to each elemental integral

$$\int_{\Omega_e} [\ \mathcal{L}u(\underset{\sim}{x})\ ]\ w_i(\underset{\sim}{x})\ d\underset{\sim}{x} \tag{3.5}$$

The result is the following equation

$$\int_{\Omega_e} (\mathcal{L}u)\ w_i(\underset{\sim}{x})\ d\underset{\sim}{x} = \int_{\Omega_e} u\ (\mathcal{L}^{*} w_i)\ d\underset{\sim}{x} + [\text{Boundary Terms}]_{\Omega_e} \tag{3.6}$$

where $\mathcal{L}^*$ is the adjoint operator associated with $\mathcal{L}$ and the "boundary terms" involve integrals around the boundary of Ω_e.

If the weight or test functions $w_i(\underset{\sim}{x})$ are chosen to satisfy the homogeneous adjoint equation $\mathcal{L}^* w_i(\underset{\sim}{x}) = 0$ within each subregion Ω_e, then, the left side of equation (3.2) reduces to

$$\int_\Omega [\ \mathcal{L}u(\underset{\sim}{x})\ ]\ w_i(\underset{\sim}{x})\ d\underset{\sim}{x} = \sum_e [\text{Boundary Terms}]_{\Omega_e} \tag{3.7}$$

This is the fundamental idea of localized adjoint methods (LAM's). Evaluation of the "boundary terms" on the right side of (3.7) produces the algebraic approximations of interest.

3.3 An ELLAM for the Advective–Diffusive–Reactive equation

Consider the single species, one–dimensional, constant coefficient, transient advective–diffusive–reactive transport equation

$$\mathcal{L}c \equiv R\frac{\partial c}{\partial t} + V\frac{\partial c}{\partial x} - D\frac{\partial^2 c}{\partial x^2} + Kc = f(x,t) \tag{3.8}$$

$$\begin{aligned} x \in \Omega_x &= (0,L), \\ t \in \Omega_t &= (0,\infty), \\ (x,t) \in \Omega_{x,t} &\equiv \Omega_x \times \Omega_t \end{aligned}$$

with suitable initial and boundary conditions,

$$c(x,0) = c_I(x) \quad 0 \le x \le L \tag{3.9a}$$

$$c(0,t) = c_0(t) \quad t > 0 \tag{3.9b}$$

$$c(1,t) = c_L(t) \quad t > 0 \tag{3.9c}$$

where $\mathcal{L}$ is the governing space–time differential operator, R is a retardation coefficient (dimensionless), c is the concentration of the dissolved substance [M/L^3], V is the fluid velocity [L/t], D is a diffusion coefficient [L^2/t]; K is a first–order reaction coefficient [1/t], f(x,t) is a given forcing function (i.e. a source/sink term) [$M/L^3 \cdot t$], x is the space dimension [L] and t is the time dimension [t].

The numerical development starts by writing the weak form of (3.8),

$$\int_{\Omega_{x,t}} (\mathcal{L}c)\, w_i(x,t)\, dx\, dt = \int_{\Omega_{x,t}} f(x,t)\, w_i(x,t)\, dx\, dt \tag{3.10}$$

where $w_i(x,t)$ is a weight or test function. The reason for weak forms can be justified as follows. The governing differential equation (3.8) admits nothing but smooth solutions c(x,t); that is solutions c(x,t) that can be (at least) differentiated two times (since the governing equation is a second order PDE). Weak forms, on the contrary, allow smooth solutions c(x,t) and solutions c(x,t) with lower or weaker smoothness constrains. Furthermore, weak forms can accommodate irregular data such as discontinuous forcing functions or coefficients, a common occurrence in practical applications (see, for example, Becker, Carey and Oden, 1983).

For the operator $\mathscr{L}$ of (3.8), the formal adjoint operator is,

$$\mathscr{L}^* w = -R\frac{\partial w}{\partial t} - V\frac{\partial w}{\partial x} - D\frac{\partial^2 w}{\partial x^2} + Kw \tag{3.11}$$

accordingly, the homogeneous adjoint equation is defined as

$$R\frac{\partial w}{\partial t} + V\frac{\partial w}{\partial x} + D\frac{\partial^2 w}{\partial x^2} - Kw = 0 \tag{3.12}$$

This equation can be satisfied in a multitude of ways. For example, consider the following set of homogeneous sub–equations of (3.12): (1) $R\frac{\partial w}{\partial t} = 0$ and $V\frac{\partial w}{\partial x} + D\frac{\partial^2 w}{\partial x^2} - Kw = 0$, (2) $R\frac{\partial w}{\partial t} + V\frac{\partial w}{\partial x} = 0$ and $D\frac{\partial^2 w}{\partial x^2} - Kw = 0$, (3) $R\frac{\partial w}{\partial t} + V\frac{\partial w}{\partial x} - Kw = 0$ and $D\frac{\partial^2 w}{\partial x^2} = 0$.

Each collection of sub–equations effectively reduces the infinite–dimensional solution space of the homogeneous adjoint equation to a finite–dimensional space. Each choice also implies a different type of test function. Consequently, many distinct algebraic approximations to the governing

differential equation can be produced using this approach. In particular, let equation (3.12) be satisfied by taking

$$R\frac{\partial w}{\partial t} + V\frac{\partial w}{\partial x} - Kw = 0 \qquad (3.13a)$$

$$D\frac{\partial^2 w}{\partial x^2} = 0 \qquad (3.13b)$$

It is clear that the second expression, (3.13b), indicates functions w that vary linearly in space, i.e., $w(x) = C_1 x + C_2$, where C_1 and C_2 are arbitrary real constants. Similarly, solving (3.13a) leads to exponentially growing (or decaying, depending on the sign of K, $K \neq 0$) functions w *along* lines with slope $1/(V/R)$. This lines are the *characteristic curves* of $\frac{\partial w}{\partial t} + (V/R)\frac{\partial w}{\partial x} - (K/R)\, w = 0$ when constant coefficients are employed. This can be shown as follows. Let $w = w(x,t)$. The material or total derivative of w corresponds to

$$\frac{Dw}{Dt} = \frac{\partial w}{\partial t} + \frac{\partial w}{\partial x}\frac{dx}{dt} \qquad (3.14)$$

Whenever $\frac{dx}{dt} = \frac{V}{R}$, the right side of equation (3.14) is, according to (3.13a), equal to $\frac{K}{R}w$. That is,

$$\frac{Dw}{Dt} = \frac{K}{R}w \qquad (3.15)$$

Integration of (3.15), i.e. solving $\int \frac{dw}{w} = K\int dt$, gives

$$w = C\, e^{\frac{K}{R}t} \qquad (3.16)$$

where C is an arbitrary real constant.

Combining these two results, namely w varying linearly along space and exponentially along characteristic lines, the following elements and associated test function are defined using a rectangular array of equally spaced nodes in space and in time,

$$w_i^{n+1}(x,t) = \begin{cases} \left[\dfrac{(x - x_{i-1})}{\Delta x} + V \dfrac{(t^{n+1} - t^n)}{\Delta x} \right] e^{K(t-t^n)}, & (x,t) \in \Omega_1^i \\ \left[\dfrac{(x_{i+1} - x)}{\Delta x} - V \dfrac{(t^{n+1} - t^n)}{\Delta x} \right] e^{K(t-t^n)}, & (x,t) \in \Omega_2^i \\ 0, & \text{all other } (x,t) \end{cases} \tag{3.17}$$

The subscript i refers to spatial location i(Δx), and the superscript n indicates time n(Δt). The test function w_i^{n+1} is illustrated in figure 3.1. Regions or elements Ω_1^i and Ω_2^i are shown in figure 3.2.

Equation (3.17) is formed by considering piecewise linear "hat" functions that "slide" along characteristic lines between time steps t^n and t^{n+1} while being subject to exponential growth or decay in time whenever K, the first–order reaction coefficient, is not equal to zero. When K = 0, w remains constant along characteristic lines and equation (3.17) reverts to the expression originally derived by Celia et al. (1989c) for non–reactive transport.

The function $w_i^{n+1}(x,t)$ has the properties that it is C^{-1} continuous in time and C^0 in space; that is, $\int_0^\infty w(t')\,dt'$ is a continuous function in time, while w is continuous over $0 \le x \le l$. The discontinuities in time are found at t^n and t^{n+1}, the beginning and end of the time step under consideration. The discontinuities

Figure 3.1 : Typical test functions $w_i^{n+1}(x,t)$, plotted over space–time regions Ω_1^i and Ω_2^i, for the cases of (A) non–reactive transport, where K = 0, and (B) reactive transport with K < 0. Note that in (B) the test function $w_i^{n+1}(x,t)$ undergoes exponential decay in time along characteristic lines.

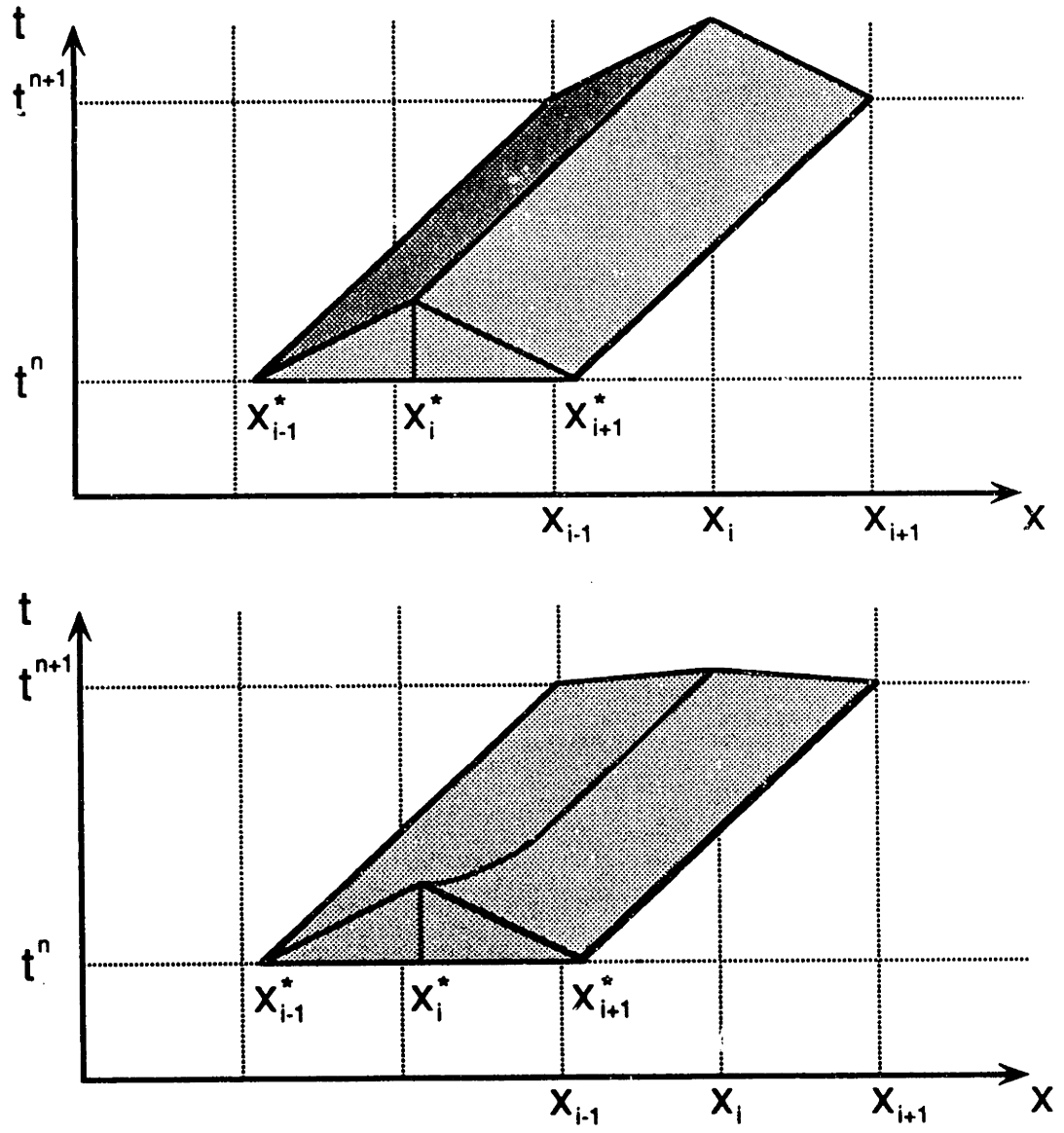

Figure 3.2 : Plot of two space–time regions Ω_1^i and Ω_2^i. The lines $x_l^i(t)$, $x_c^i(t)$, $x_r^i(t)$ coincide with the characteristics that intersect the nodes x_{i-1}, x_i, and x_{i+1} at time level t^{n+1}.

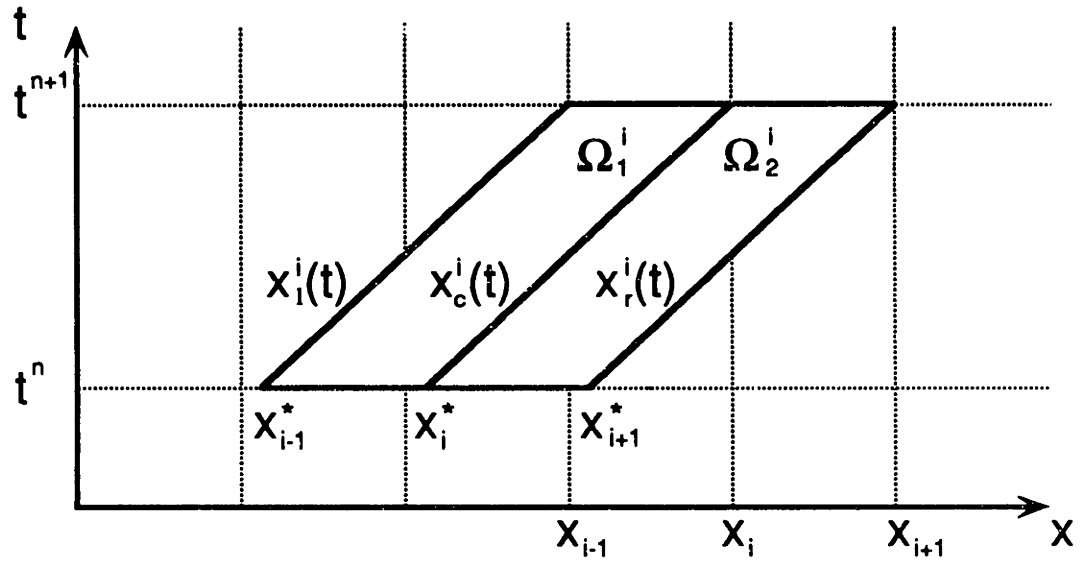

in space, in the derivative of $w_i^{n+1}(x,t)$, i.e. $\frac{\partial w_i^{n+1}}{\partial x}$, coincide with the characteristic lines $x_l^i(t)$, $x_c^i(t)$ and $x_r^i(t)$, shown in figure 3.2. This lines, $x_l^i(t)$, $x_c^i(t)$ and $x_r^i(t)$, intersect time $t = t^n$ at locations x_{i-1}^*, x_i^*, x_{i+1}^*, respectively, which are referred to as the "foot of the characteristic" points.

The next step in the ELLAM procedure consists of writing the left side of (3.10) as an equivalent sum of elemental integrals,

$$\int_{\Omega_{x,t}} (\mathscr{L}c)\, w_i^{n+1}(x,t)\, dx\, dt = \sum_{e=1}^{E} \int_{\Omega_e} (\mathscr{L}c)\, w_i^{n+1}(x,t)\, dx\, dt \qquad (3.18)$$

Equation (3.18) is an equality whenever the integral on the left side is bounded at all points in $\Omega_{x,t}$. This occurs, for example, for $c(x,t) \in \mathbb{C}^1[\Omega_x], \mathbb{C}^0[\Omega_t]$. However, for $c(x,t) \in \mathbb{C}^0[\Omega_{x,t}]$ equation (3.18) must be modified to account for the unbounded nature of the second derivative $\frac{\partial^2 c}{\partial x^2}$ in $(\mathscr{L}c)$.

Let $c(x,t)$ be $\mathbb{C}^0[\Omega_{x,t}]$. Note that the left side of (3.18) can be expressed as

$$\int_{\Omega_{x,t}} (\mathscr{L}c)\, w_i^{n+1}(x,t)\, dx\, dt =$$

$$\int_0^\infty \int_0^L \left(R \frac{\partial c}{\partial t} + V \frac{\partial c}{\partial x} + Kc\right) w_i^{n+1}\, dx\, dt - \int_0^\infty \int_0^L D \frac{\partial^2 c}{\partial x^2} w_i^{n+1}\, dx\, dt \qquad (3.19)$$

The last term of equation (3.19) is equal to

$$\int_0^{\infty}\int_0^{L} D\,\frac{\partial^2 c}{\partial x^2}\,w_i^{n+1}\,dx\,dt = D\int_{t^n}^{t^{n+1}} \lim_{\epsilon\to 0}\left\{ \sum_{j=0}^{E-1} \int_{x_j(t)+\epsilon}^{x_{j+1}(t)-\epsilon} \frac{\partial^2 c}{\partial x^2}\,w_i^{n+1}\,dx \right.$$

$$\left. + \sum_{j=1}^{E-1} \int_{x_j(t)-\epsilon}^{x_j(t)+\epsilon} \left(\frac{\partial c}{\partial x}\Big|_{x_j(t)+\epsilon} - \frac{\partial c}{\partial x}\Big|_{x_j(t)-\epsilon} \right) \delta[x - x_j(t)]\,w_i^{n+1}\,dx \right\} dt \qquad (3.20)$$

where $x_j(t)$ is the vertical line (parallel to the time axis) extending from (x_j,t^n) to (x_j,t^{n+1}) and $\delta[x - x_j(t)]$ is the Dirac delta function acting along $x_j(t)$.

Equation (3.20) may now be substituted into the last term of (3.19) to produce the following equivalent sum of elemental integrals

$$\int_{\Omega_{x,t}} (\mathscr{L}c)\,w_i^{n+1}(x,t)\,dx\,dt =$$

$$\sum_{e=1}^{E} \int_{\Omega_e} \left(R\,\frac{\partial c}{\partial t} + V\,\frac{\partial c}{\partial x} + Kc\right) w_i^{n+1}\,dx\,dt - \sum_{e=1}^{E} \int_{\mathring{\Omega}_e} D\,\frac{\partial^2 c}{\partial x^2}\,w_i^{n+1}\,dx\,dt$$

$$- \lim_{\epsilon\to 0}\left\{ D\int_{t^n}^{t^{n+1}} \sum_{j=1}^{E-1} \left(\frac{\partial c}{\partial x}\Big|_{x_j(t)+\epsilon} - \frac{\partial c}{\partial x}\Big|_{x_j(t)-\epsilon} \right) w_i^{n+1}[x_j(t),t]\,dt \right\} \qquad (3.21)$$

The second sum in equation (3.21) corresponds to integration interior to each element Ω_e, where $c(x,t) \in \mathbb{C}^{\infty}[\Omega_{x,t}]$. The third sum is the evaluation of the Dirac delta function acting along vertical lines $x_j(t)$.

Application of integration by parts to the right side of (3.21) yields

$$\int_0^{\infty}\int_0^{L} (\mathscr{L}c)\,w_i^{n+1}(x,t)\,dx\,dt =$$

$$\int_{x_{i-1}}^{x_{i+1}} c(x,t^{n+1})\, w_i^{n+1}(x,t^{n+1})\, dx \;-\; \int_{x_{i-1}}^{x^*_{i+1}} c(x,t^{n})\, w_i^{n+1}(x,t^{n})\, dx$$

$$- D\left\{ \int_{t^n}^{t^{n+1}} c[x_l^i(t),t] \left[\!\left[\frac{\partial w_i^{n+1}}{\partial x} \right]\!\right]_{x_l^i(t)} dt \;+\; \int_{t^n}^{t^{n+1}} c[x_c^i(t),t] \left[\!\left[\frac{\partial w_i^{n+1}}{\partial x} \right]\!\right]_{x_c^i(t)} dt \right.$$

$$\left. + \int_{t^n}^{t^{n+1}} c[x_r^i(t),t] \left[\!\left[\frac{\partial w_i^{n+1}}{\partial x} \right]\!\right]_{x_r^i(t)} dt \right\}$$

$$= \int_{\Omega_1^i + \Omega_2^i} f(x,t)\, w_i^{n+1}(x,t)\, dx\, dt \qquad (3.22)$$

where the double bracket $\left[\!\left[\cdot \right]\!\right]_{x_k}$ indicates a spatial jump operator, defined as $\lim_{\epsilon \to 0} [\,(\cdot)|_{x_k + \epsilon} - (\cdot)|_{x_k - \epsilon}\,]$.

In equation (3.22) use was made of the fact that $\mathscr{L}^* w_i^{n+1} = 0$ within each subregion Ω_j^i, j = 1, 2; i = 0, 1, 2, ..., E, to eliminate all interior integrals.

The spatial jump operator of (3.22) can be evaluated explicitly from equation (3.17) as

$$\left[\!\left[\frac{\partial w_i^{n+1}}{\partial x} \right]\!\right]_{x_l^i(t)} = \frac{e^{K(t-t^n)}}{\Delta x} \qquad (3.23a)$$

$$\left[\!\left[\frac{\partial w_i^{n+1}}{\partial x} \right]\!\right]_{x_c^i(t)} = -\frac{2e^{K(t-t^n)}}{\Delta x} \qquad (3.23b)$$

$$\left[\frac{\partial w_i^{n+1}}{\partial x}\right]_{x_r^i(t)} = \frac{K(t-t^n)}{\frac{e}{\Delta x}} \qquad (3.23c)$$

Finally, equations (3.22) and (3.23a)–(3.23c) can be combined to produce a general algebraic approximation to the governing differential equation.

In deriving (3.22) an assumption was made that the characteristic lines do not intersect the spatial boundary. When one or more of the characteristic lines $x_l^i(t)$, $x_c^i(t)$, $x_r^i(t)$ intersects the spatial boundary, equation (3.22) must be modified (see figures 3.3 and 3.4). This happens for nodes i = 0, 1, ..., Nc+1, where Nc = Trunc(Cu). When this modification is performed, boundary conditions are introduced into the approximating equations. Celia et al. (1989c) have shown that proper treatment of both inflow and outflow boundaries provides a formulation that demonstrably conserves global mass. Detailed discussion and illustration of boundary condition implementation can be found in that paper. The derivation is not repeated here.

Consider a choice of the unknown function c(x,t) such that,

$$c(x,t^n) = \sum_{j=0}^{E} C_j^n \, \phi_j(x) \qquad (3.24a)$$

$$c(x,t^{n+1}) = \sum_{j=0}^{E} C_j^{n+1} \, \phi_j(x) \qquad (3.24b)$$

where $\phi_j(x)$ are standard piecewise Lagrange polynomials and $C_j^n \simeq c(x_j,t^n)$, $C_j^{n+1} \simeq c(x_j,t^{n+1})$ indicate approximate nodal values. Given definitions (3.24a)–(3.24b) the integrals in (3.22) can be evaluated as,

Figure 3.3 : Space–time region Ω_2^0 meeting an inlet boundary. Shape for (A) $0 \leq Cu \leq 1$, and (B) $Cu \geq 1$. Cu ($\equiv \frac{V\Delta t}{\Delta x}$) denotes the grid Courant number.

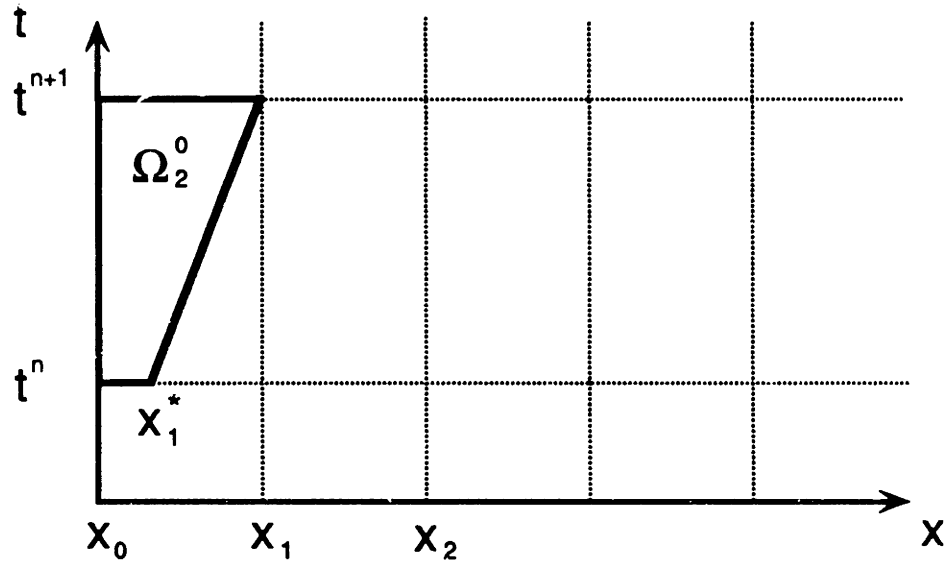

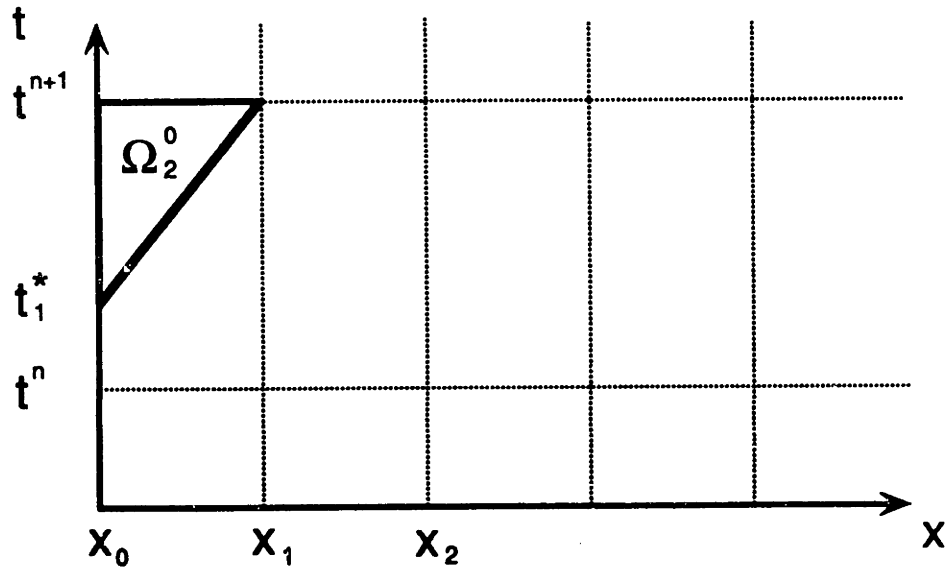

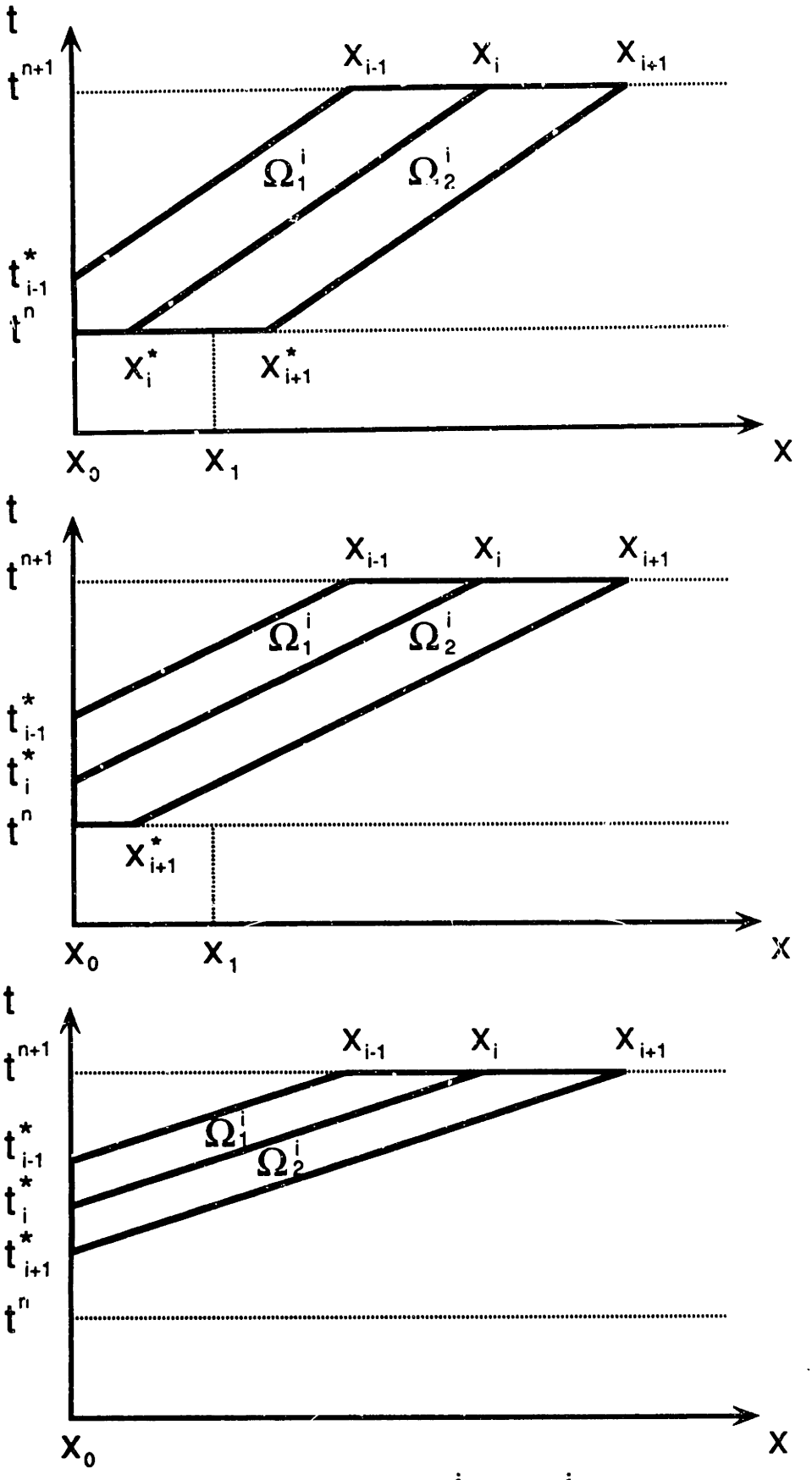

Figure 3.4 : Typical space–time regions Ω_1^i and Ω_2^i $(i \geq 1)$ meeting an inlet boundary. Shapes for (A) $i-1 \leq Cu \leq i$, (B) $i \leq Cu \leq i+1$ and (C) $Cu \geq i+1$.

$$\int_{x_{i-1}}^{x_{i+1}} c(x,t^{n+1})\, w_i^{n+1}(x,t^{n+1})\, dx =$$

$$\Delta x\, e^{K\Delta t} \left(\frac{1}{6} C_{i-1}^{n+1} + \frac{2}{3} C_i^{n+1} + \frac{1}{6} C_{i+1}^{n+1} \right) \quad (3.25a)$$

$$\int_{x_{i-1}}^{x_{i+1}^*} c(x,t^n)\, w_i^{n+1}(x,t^n)\, dx =$$

$$\Delta x \left(\beta_1 C_m^n + \beta_2 C_{m+1}^n + \beta_3 C_{m+2}^n + \beta_4 C_{m+3}^n \right) \quad (3.25b)$$

$$\int_{t^n}^{t^{n+1}} c[x_f^i(t),t] \frac{e^{K(t-t^n)}}{\Delta x}\, dt =$$

$$\gamma \frac{\Delta t}{\Delta x} \left[(1-\theta)(1-\alpha)\, C_m^n + (1-\theta)\alpha\, C_{m+1}^n + \theta\, C_{i-1}^{n+1} \right] \quad (3.25c)$$

$$\int_{t^n}^{t^{n+1}} c[x_c^i(t),t] \left(-\frac{2e^{K(t-t^n)}}{\Delta x} \right) dt =$$

$$-2\gamma \frac{\Delta t}{\Delta x} \left[(1-\theta)(1-\alpha)\, C_{m+1}^n + (1-\theta)\alpha\, C_{m+2}^n + \theta\, C_i^{n+1} \right] \quad (3.25d)$$

$$\int_{t^n}^{t^{n+1}} c[x_r^i(t),t] \frac{e^{K(t-t^n)}}{\Delta x}\, dt =$$

$$\gamma \frac{\Delta t}{\Delta x} \left[(1-\theta)(1-\alpha)\, C_{m+2}^n + (1-\theta)\alpha\, C_{m+3}^n + \theta\, C_{i+1}^{n+1} \right] \quad (3.25e)$$

where the terms β_1, β_2, β_3, β_4 result from an exact evaluation of the integral in (3.25b) at $t = t^n$,

$$\beta_1 = \frac{1}{6} - \frac{\alpha}{2} + \frac{\alpha^2}{2} - \frac{\alpha^3}{6},$$

$$\beta_2 = \frac{2}{3} - \alpha^2 + \frac{\alpha^3}{2},$$

$$\beta_3 = \frac{1}{6} + \frac{\alpha}{2} + \frac{\alpha^2}{2} - \frac{\alpha^3}{2},$$

$$\beta_4 = \frac{\alpha^3}{6},$$

$\alpha \equiv 1 - (Cu - Nc)$, and,

$m \equiv i - Nc - 2$,

Nc is the truncated integer value of the Courant number Cu ($\equiv \frac{V\Delta t}{\Delta x}$),

$$\gamma \equiv \frac{(e^{K\Delta t} - 1)}{K\Delta t},$$

θ is a time weighting parameter, usually taken as $0 \leq \theta \leq 1$.

Substitution of equations (3.25a)–(3.25e) into (3.22) with f = 0 yields the following discrete approximation for node i, Nc + 1 < i < E,

$$C_{i-1}^{n+1}\left[\frac{e^{K\Delta t}}{6} - \rho\gamma\theta\right] + C_i^{n+1}\left[\frac{2e^{K\Delta t}}{3} + 2\rho\gamma\theta\right] + C_{i+1}^{n+1}\left[\frac{e^{K\Delta t}}{6} - \rho\gamma\theta\right]$$

$$= C_m^n\left[\beta_1 + \rho\gamma(1-\theta)(1-\alpha)\right] + C_{m+1}^n\left[\beta_2 + \rho\gamma(1-\theta)(3\alpha-2)\right]$$

$$+ C_{m+2}^n\left[\beta_3 + \rho\gamma(1-\theta)(1-3\alpha)\right] + C_{m+3}^n\left[\beta_4 + \rho\gamma(1-\theta)\alpha\right] \qquad (3.26)$$

in which ρ is the dimensionless diffusivity, defined as $\frac{D\Delta t}{(\Delta x)^2}$.

The discrete approximation of equation (3.26) is a specific example of the general equation (3.22). Other approximations may be derived by considering different approximations to the integrals in (3.22).

Chapter 4: NUMERICAL EXAMPLES

4.1 Introduction

This chapter is intended to demonstrate the performance of the Eulerian–Lagrangian localized adjoint method (ELLAM) in solving mass transport problems in advection–dominated flows (high Peclet numbers). To this end, three *test problems* are considered: (1) advective–diffusive propagation of an initial step discontinuity, (2) advective–only propagation and advective–diffusive propagation of a Gauss hill, and (3) advective–diffusive–reactive propagation of a step front.

Various *test cases* – involving distinct parameters (e.g. Velocity, Δx, Δt, etc.) and boundary conditions (e.g. Dirichlet or first type, Neumann or second type) – are solved for the problems mentioned above: test cases 1 through 6 correspond to the propagation of an initial step discontinuity, 7 through 21 to the propagation of a Gauss hill, and 22 through 27 to the non–conservative propagation of a step front. Tables 4.2, 4.3 and 4.4 provide a listing of these test cases.

The tests were designed to examine, in particular, (1) the effect of the Courant number and (2) the ability of the ELLAM to handle boundary conditions.

Several error measures, shown in Table 4.1, provide a quantitative basis for the analysis of the results. They include: (1) the L2 error norm, an integral measure of the overall error of the numerical solution, (2) the error in the peak concentration (ϵ), a point measure of artificial damping, (3) the value of the

maximum negative concentration (ψ), a point measure of spurious oscillations (wiggles), and (4) the 0^{th} moment of the concentration profile (μ_0), an integral measure of mass preservation.

The governing equation solved in all cases is

$$\mathcal{L}c \equiv R\frac{\partial c}{\partial t} + V\frac{\partial c}{\partial x} - D\frac{\partial^2 c}{\partial x^2} + Kc = 0 \qquad (4.1)$$

$$\begin{aligned} x \in \Omega_x &= (0,1), \\ t \in \Omega_t &= (0,\infty), \\ (x,t) \in \Omega_{x,t} &\equiv \Omega_x \times \Omega_t \end{aligned}$$

subject to initial and boundary conditions that are defined in each simulation.

Table 4.1: Error Measures

Symbol	Description	Comments	Value for Exact Solution
–	L2 Error Norm	Integral measure of the overall error of the numerical solution	0
ϵ	Error in the peak concentration, normalized by the exact peak concentration	Point measure of the artificial damping of the numerical solution (numerical damping)	0
ψ	Value of the maximum negative concentration, normalized by the exact peak concentration	Point measure of the spurious oscillations in the numerical solution (wiggles)	0
μ_0	0^{th} moment of the concentration profile, normalized by the exact value	Integral measure of mass preservation	1

Table 4.1: (cont.)

Definitions

$$\text{L2 Error Norm (t)} = \left[\int_0^1 [e(x,t)]^2 \, dx \right]^{1/2}$$

where

$$e(x,t) = c^{ex}(x,t) - c^{nu}(x,t)$$

and

$c^{nu}(x,t)$ is a piecewise linear function

$$\epsilon\,(t) = \frac{c^{ex}_{max}(t) - c^{nu}_{max}(t)}{c^{ex}_{max}(t)}$$

$$\psi\,(t) = \frac{c^{nu}_{max,negative}(t)}{c^{ex}_{max}(t)}$$

$$\mu_0(t) = \frac{\int_0^1 c^{nu}(x,t)\ dx}{\int_0^1 c^{ex}(x,t)\ dx}$$

Note: All reported error measurements were evaluated at $t = t^f$.

Table 4.2: Test Cases for the Propagation of an Initial Step Discontinuity

Test	Time Steps	t^0	t^f	Velocity	Courant Number	Peclet Number	Figure
1*	40	0	0.40	1.00	0.50	100	4.1
2*	40	0	0.40	1.66	0.83	166	4.2
3	40	0	0.40	2.00	**1.00**	200	4.3
. . . . .							
4	4	0	0.04	10.00	**5.00**	1000	4.4
5	4	0	0.04	16.60	8.30	1660	4.5
6	4	0	0.04	20.00	**10.00**	2000	4.6

Error Measurements

Test	L2 Error Norm	ε	ψ	μ_0
1*	0.040396	−0.025996	−0.036437	1.019115
2*	0.046058	−0.015326	−0.057853	1.013681
3	**0.044810**	**−0.003966**	**−0.004885**	**1.012287**
. . . . .				
4	**0.067397**	**−0.010662**	**−0.009724**	**1.025048**
5	0.061161	−0.083939	−0.052362	1.015110
6	**0.067453**	**−0.010257**	**−0.009736**	**1.012546**

* Graphical results for this case – using the OTF numerical solution procedure – are presented in Celia et al., 1989a.

Table 4.3: Test Cases for the Propagation of a Gauss Hill

Test	Time Steps	t^o	t^f	Velocity	Courant Number	Peclet Number	Figure
7	25	0	0.25	1.66	0.83	∞	4.7
8	25	0	0.25	2.00	**1.00**	∞	4.8
9	2	0	0.02	16.60	8.30	∞	4.9
10	2	0	0.02	20.00	**10.00**	∞	4.10
11*	25	0	0.25	0.50	0.25	500	4.11
12*	25	0	0.25	1.00	0.50	1000	4.12
13*	25	0	0.02	1.66	0.83	1660	4.13
14	25	0	0.02	2.00	**1.00**	2000	4.14
15	2	0	0.02	16.60	8.30	16600	4.15
16	2	0	0.02	20.00	**10.00**	20000	4.16
17	15	0	0.15	6.00	**3.00**	12	4.17
18	15	0	0.15	5.50	2.75	1100	4.18
19	15	0	0.15	6.00	**3.00**	1200	4.19
20	25	0	0.25	1.00	0.50	1000	4.20
21	25	0	0.02	2.00	**1.00**	2000	4.21

Table 4.3 (cont.)

Error Measurements

Test	L2 Error Norm	ξ	ψ	μ_0
7	0.008542	0.014212	–0.000016	1.000000
8	**0.006793**	**0.000000**	**0.000000**	**1.000000**
9	0.007060	0.001996	0.000000	1.000000
10	**0.006793**	**0.000000**	**0.000000**	**1.000000**
11*	0.009640	0.020809	–0.000064	1.000000
12*	0.011549	0.029863	–0.000029	1.000000
13*	0.008459	0.014088	–0.000015	1.000000
14	**0.006775**	**0.000339**	**0.000000**	**1.000000**
15	0.007055	0.002005	0.000000	1.000000
16	**0.006792**	**0.000027**	**0.000000**	**1.000000**
17a	**0.010781**	**0.061421**	**0.000000**	**0.999972**
17b	**0.001265**	**–0.005120**	**–0.000007**	**0.999960**
18a	0.052911	0.231589	–0.004421	0.998687
18b	0.005204	–0.015427	–0.000071	1.000408
19a	**0.041000**	**0.014066**	**–0.000058**	**1.002253**
19b	**0.005391**	**–0.015320**	**–0.000001**	**1.000249**
20	0.011549	0.029863	–0.000029	1.000000
21	**0.006776**	**0.000325**	**0.000000**	**1.000000**

* Graphical results for this case – using the OTF numerical solution procedure – are presented in Celia et al., 1989a.

Table 4.4: Test Cases for the Advective–Diffusive–Reactive Propagation of a Step Front.

Test	Time Steps	t^f	Velocity	Courant Number	Peclet Number	R	K	Figure
22	40	4.0	0.166	0.83	20	1	0.166	4.22
23	40	4.0	0.200	**1.00**	20	1	0.200	4.23
...								
24	4	0.4	1.660	8.30	20	1	1.660	4.24
25	4	0.4	2.000	**10.00**	20	1	2.000	4.25
...								
26	40	4.0	0.166	0.83	20	2	0.166	4.22
27	40	4.0	0.200	**1.00**	20	2	0.200	4.23

Error Measurements

Test	L2 Error Norm	ε	ψ	μ_0
22	0.013567	0.000000	0.000000	1.006760
23	0.011623	0.000000	−0.000025	1.003300
...				
24	0.048078	0.000000	0.000000	0.939445
25	0.060408	0.000000	0.000000	0.921704
...				
26	0.020411	0.000000	−0.003676	1.020515
27	0.018691	0.000000	−0.001544	1.016364

4.2 Propagation of an Initial Step Discontinuity

This test consists of solving equation (4.1) with R = 1 and K = 0, with initial condition

$$c(x,t) = 0, \quad 0 < x < l, \quad t = 0 \tag{4.2}$$

and boundary conditions

$$c(0,t) = 1, \quad t > 0, \tag{4.3a}$$

$$c(l,t) = 0, \quad t > 0, \text{ where } l \to \infty \tag{4.3b}$$

When $0 \leq x \leq l$, $l \to \infty$, $t > 0$, the analytical solution is given by

$$c(x,t) = \frac{1}{2}\,\mathrm{erfc}\left(\frac{x - Vt}{2\sqrt{Dt}}\right) + \frac{1}{2}\exp\left(\frac{Vx}{D}\right)\mathrm{erfc}\left(\frac{x + Vt}{2\sqrt{Dt}}\right) \tag{4.4}$$

For this problem, 6 test cases are considered; that is, cases 1 through 6. Each of these cases uses $\Delta x = 0.02$, $\Delta t = 0.01$, $D = 0.0002$, and time weighting parameter $\theta = 0.5$.

The ELLAM performs very well in all six cases, except that the numerical solutions tend to be slightly ahead of the analytical results. The reason for this minor inaccuracy is that the initial condition actually used in the numerical simulations is not the discontinuous step front assumed by the analytical solution; that is, the analytical solutions apply

$$c(0,t) = H(t-0) = \begin{cases} 0, & t < 0 \\ 1, & t > 0 \end{cases}$$

$$\frac{\partial c}{\partial t}(0,t) = \delta(t-0)$$

$$c(x,0) = 0, \quad 0 < x \leq 1$$

where $H(t-0)$ is the Heaviside step function and $\delta(t-0)$ is the Dirac delta function, while the numerical simulations adopt

$$c(0,t) = 1, \quad t \geq 0$$

$$\frac{\partial c}{\partial t}(0,t) = 0, \quad t \geq 0$$

$$c(x,0) = \begin{cases} 1 - \frac{x}{\Delta x}, & 0 \leq x \leq \Delta x \\ 0, & \Delta x \leq x \leq 1 \end{cases}$$

Test cases 1, 2 and 3 (see figures 4.1, 4.2, 4.3) use small Courant numbers: 0.50, 0.83 and 1, respectively. Results demonstrate that the best numerical solution is obtained for Cu = 1; i.e., an *integer* Courant number. This is because for integer Courant numbers, no approximation is used to determine the value of $c(x,t)$ at x^*_{i-1}, x^*_i and x^*_{i+1} – the "foot of the characteristics" points associated with test function w^{n+1}_i – since these positions coincide with nodes x_{i-1-Nc}, x_{i-Nc}, x_{i-Nc+1} at $t = t^n$, where Nc = Trunc(Cu), respectively. For non–integer Courant numbers (i.e. Cu ≠ Nc) a linear interpolation is employed to establish $c(x^*_{i-1},t^n)$, $c(x^*_i,t^n)$, $c(x^*_{i+1},t^n)$, and so, errors are introduced into the numerical solution.

Test cases 4 through 6 (figures 4.4, 4.5, 4.6) show that as long as integer Courant numbers are used (even if Cu >> 1), the ELLAM provides results that agree very well with the analytical solutions.

Figure 4.1: Results of test case 1 ($t^f = 0.40$). Solid curves indicate analytical solution values; dashed lines corresponds to the ELLAM numerical solution.

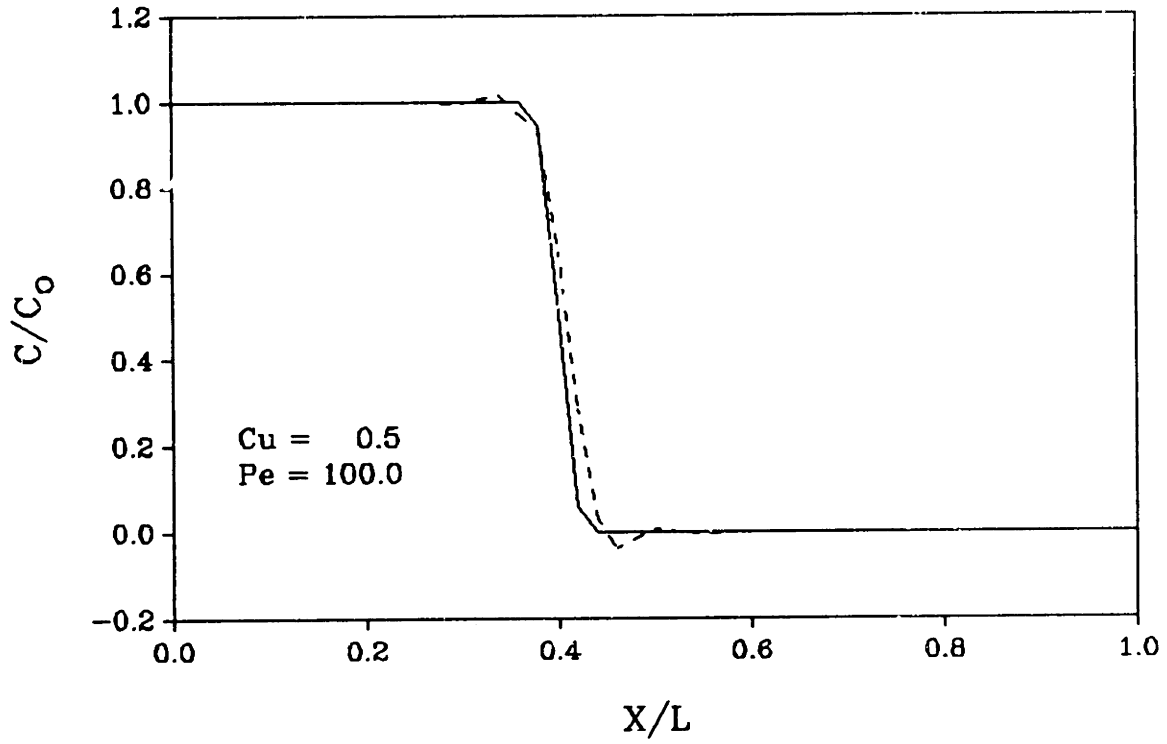

L2 Error Norm	ε	ψ	μ_0
0.040396	-0.025996	-0.036437	1.019115

Figure 4.2: Results of test case 2 ($t^f = 0.40$). Solid curves indicate analytical solution values; dashed lines corresponds to the ELLAM numerical solution.

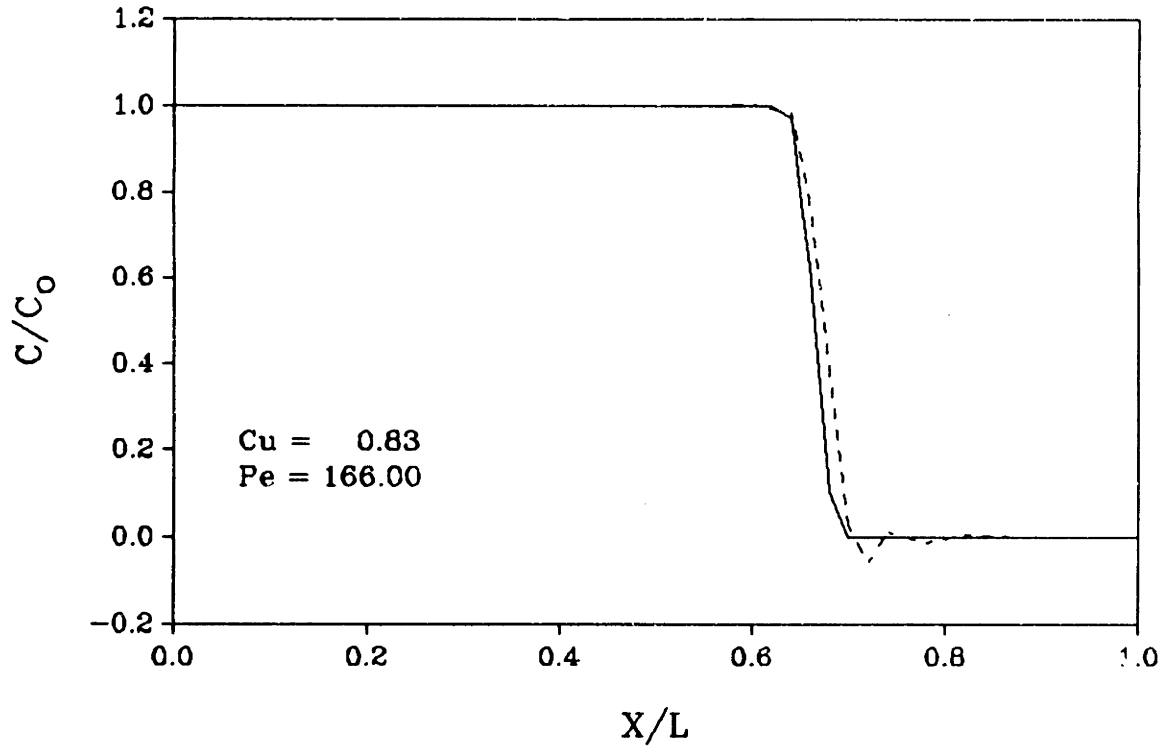

L2 Error Norm	ε	ψ	μ_0
0.046058	−0.015326	−0.057853	1.013681

Figure 4.3: Results of test case 3 ($t^f = 0.40$). Solid curves indicate analytical solution values; dashed lines corresponds to the ELLAM numerical solution.

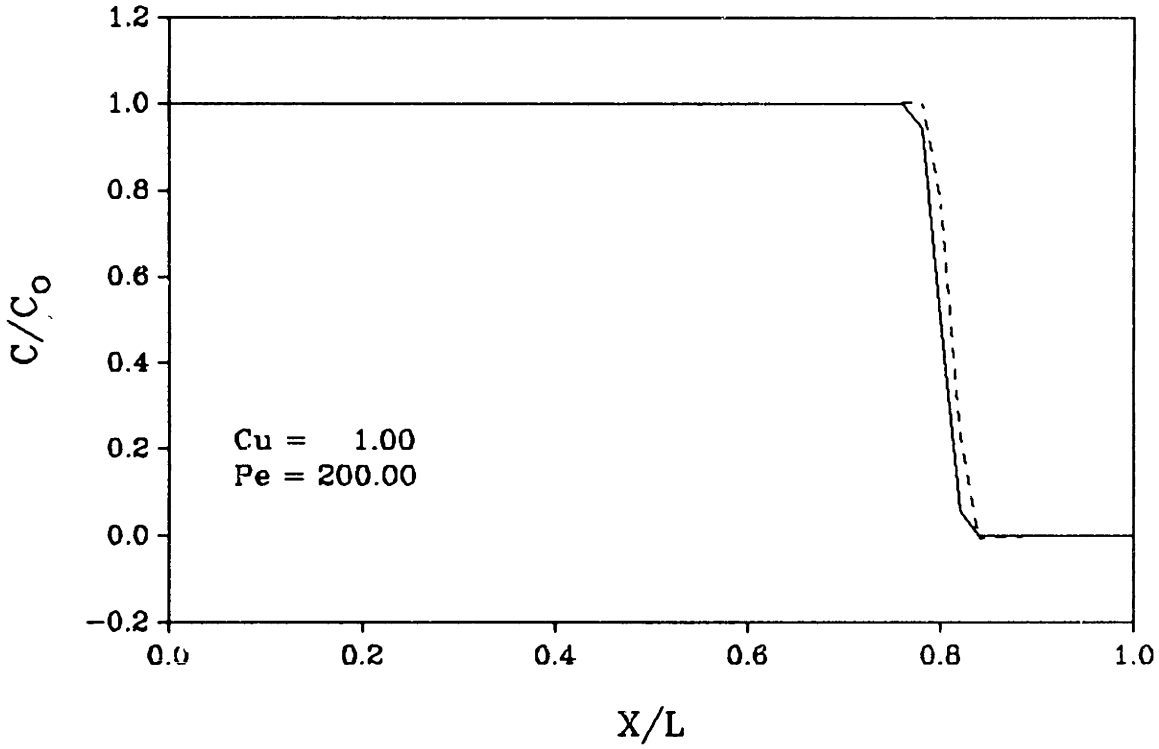

L2 Error Norm	ε	ψ	μ_0
0.044810	-0.003966	-0.004885	1.012287

Figure 4.4: Results of test case 4 ($t^f = 0.04$). Solid curves indicate analytical solution values; dashed lines corresponds to the ELLAM numerical solution.

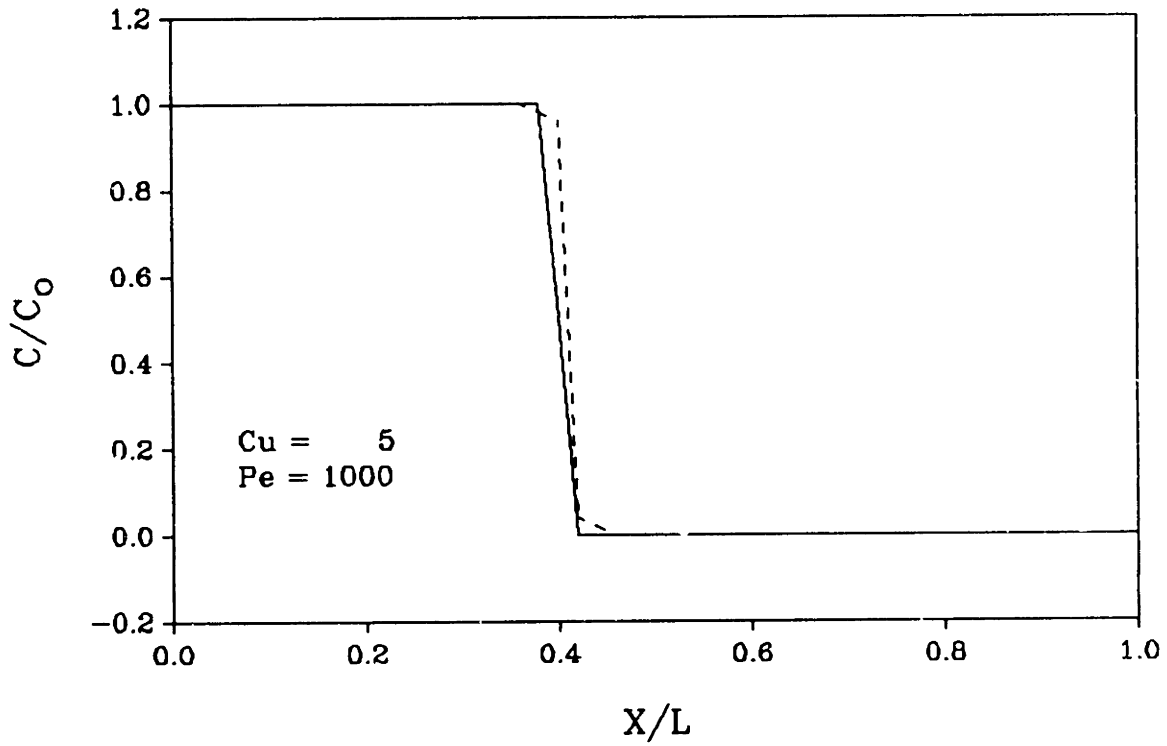

L2 Error Norm	ε	ψ	μ_0
0.067397	-0.010662	-0.009724	1.025048

Figure 4.5: Results of test case 5 ($t^f = 0.04$). Solid curves indicate analytical solution values; dashed lines corresponds to the ELLAM numerical solution.

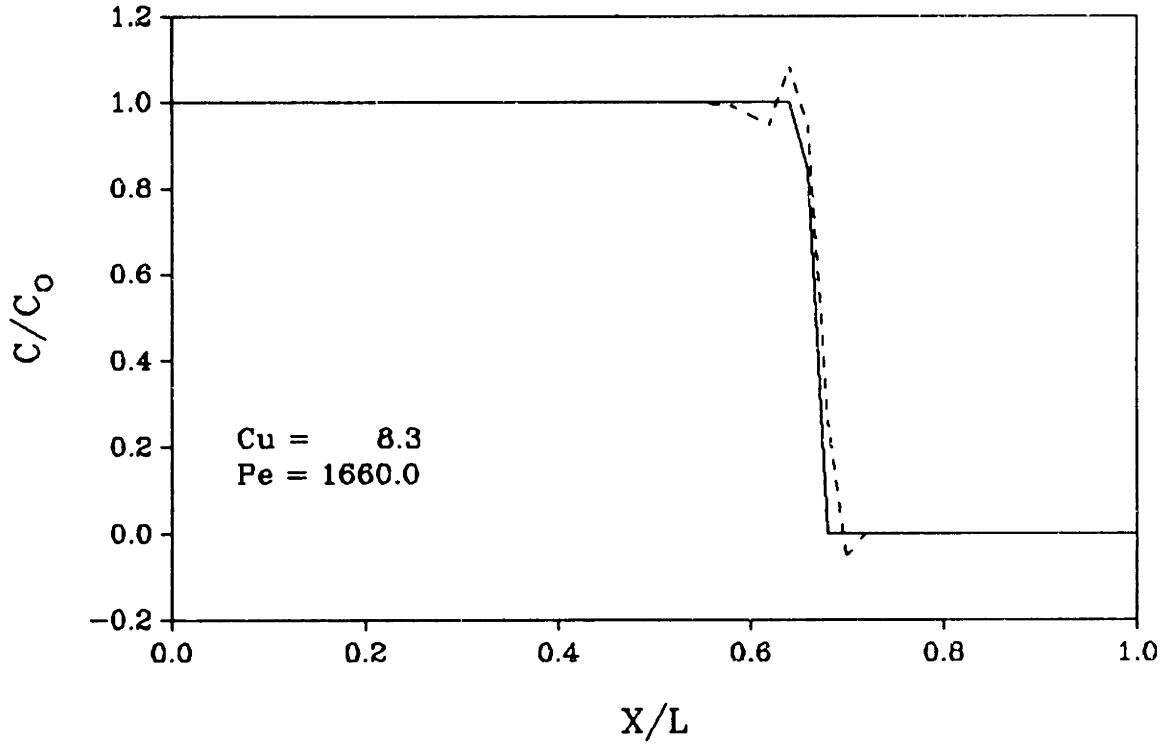

L2 Error Norm	ε	ψ	μ_0
0.061161	-0.083939	-0.052362	1.015110

Figure 4.6: Results of test case 6 ($t^f = 0.04$). Solid curves indicate analytical solution values; dashed lines corresponds to the ELLAM numerical solution.

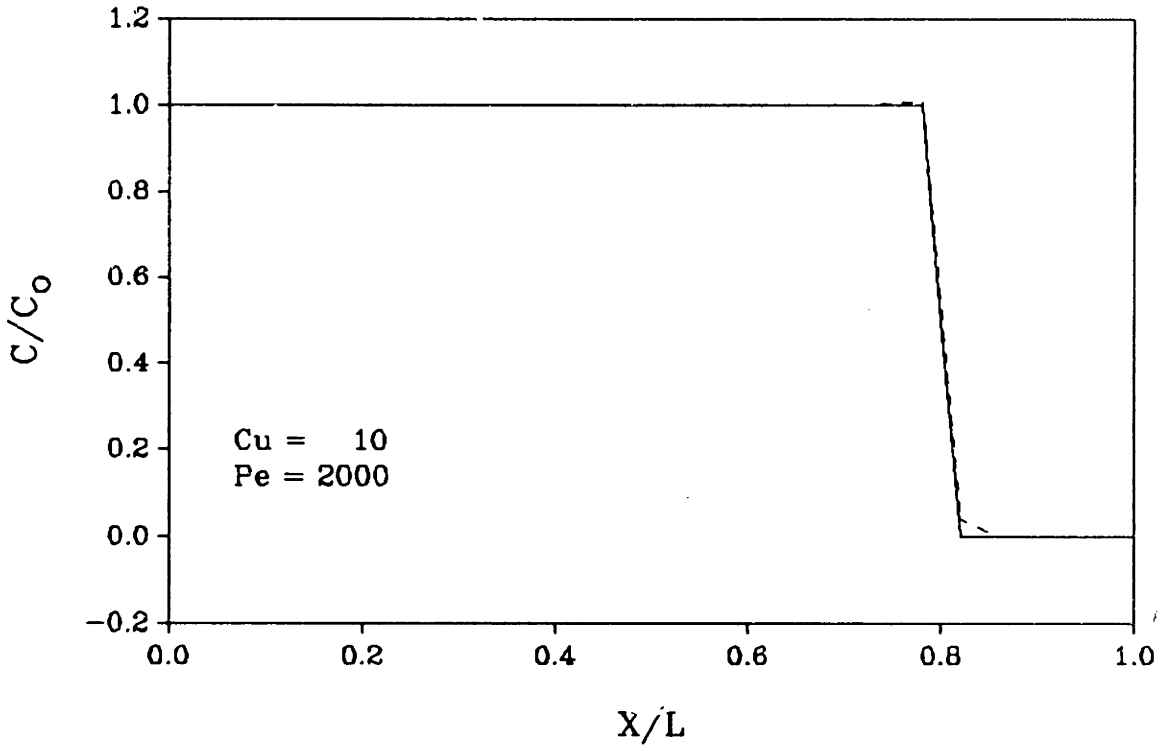

L2 Error Norm	ε	ψ	μ_0
0.067453	−0.010257	−0.009736	1.012546

4.3 Propagation of a Gauss hill

This example is defined by equation (4.1) with R = 1 and K = 0, with initial condition

$$c(x,t) = \exp\left(\frac{-(x - x_0)^2}{2\sigma_0^2} \right), \quad -\infty < x < \infty, \quad t = 0 \tag{4.5}$$

and boundary conditions

$$c(x,t) = 0, \quad |x| \to \infty, \quad t > 0 \tag{4.6}$$

where x_0 is the initial location of the center of mass, and σ_0 is the standard deviation of the initial concentration distribution.

When D = 0 (pure advection), the exact solution corresponds to the undisturbed transport of the source; that is,

$$c(x,t) = \exp\left(\frac{-(x - \bar{x})^2}{2\sigma_0^2} \right), \quad -\infty < x < \infty, \quad t \geq 0 \tag{4.7}$$

where

$$\bar{x} = x_0 + Vt$$

When D ≠ 0 (advective–diffusive transport), the correct concentration is given by

$$c(x,t) = \left(\frac{\sigma_0}{\sigma_x} \right) \exp\left(\frac{-(x - \bar{x})^2}{2\sigma_x^2} \right), \quad -\infty < x < \infty, \quad t \geq 0 \tag{4.8}$$

in which

$$\bar{x} = x_0 + Vt, \quad \sigma_x^2 = \sigma_0^2 + 2Dt$$

For this problem, 15 test cases are considered; that is, cases 7 through 21. Each of these cases uses $\Delta x = 0.02$, $\Delta t = 0.01$, $\sigma_0 = 0.0333$, and time weighting parameter $\theta = 0.5$.

Tests 7 through 16 examine the influence of the Courant number in the predictive capabilities of the ELLAM. The initial condition for these examples corresponds to (4.5) with x_0 set to 0.25. A Dirichlet boundary condition is imposed at both the inflow ($x = 0$) and outflow ($x = 1$) spatial boundaries. The simulation is stopped before the outflow boundary influences the solution.

Cases 7, 8, 9 and 10 deal with the advection–only propagation of the Gauss hill, in which $D = 0$. The ELLAM produces exact nodal values whenever $D = 0$ and an *integer* Courant number is used. This is observed in tests 8 and 10 were $\epsilon = \psi = 0$ and $\mu_0 = 1$ (for definitions see table 4.1). The L2 error norm is not zero in these examples because $c^{nu}(x,t)$ is calculated using piecewise linear functions, while the exact solution is not a polynomial function.

Cases 11 through 16 (figures 4.11, 4.12, 4.13, 4.14, 4.15 and 4.16) use $D = 0.00002$. Once more, best outcomes are obtained for integer Courant numbers (for an explanation, see paragraph 4.2).

Cases 17 through 21 investigate the ability of the ELLAM to handle boundary conditions. In tests 17, 18 and 19, a Dirichlet boundary condition (that takes values from the analytical solution) is imposed at $x = 0$ and $x = 1$. The initial condition corresponds to (4.5) with $x_0 = -0.25$. This means that the center of mass of the Gauss hill is initially located outside the domain, as shown in figure 4.16a.

Examples 17, 18 and 19 may be the most interesting in that they show the influence of the term $\frac{\partial c}{\partial x}(0,t)$ in calculating the solutions. The ELLAM numerical procedure differs from traditional Eulerian–Lagrangian methods (ELM's) in that it requires knowledge of the term $\frac{\partial c}{\partial x}(0,t)$ regardless of the type of boundary condition imposed. Thus, information on the diffusive flux at the inflow boundary – namely $\frac{\partial c}{\partial x}(0,t)$ – is necessary even when a Dirichlet problem is being considered. See Celia et al. (1989c) for details.

Test cases 17b, 18b and 19b (figures 4.17b, 4.18b, 4.19b) are solved using the ELLAM numerical procedure. Cases 17a, 18a and 19a (figures 4.17a, 4.18a, 4.19a), in contrast, result from applying an *altered* ELLAM that neglects $\frac{\partial c}{\partial x}(0,t)$, much in the form of conventional ELM's. This is accomplished in the following way: the ELLAM equation (see chapter 3, equation 3.22) associated with test function $w_i^{n+1}(x,t)$ must be modified when one or more of the characteristic lines $x_l^i(t)$, $x_c^i(t)$, $x_r^i(t)$ intersects the inflow spatial boundary. This happens for i = 0, 1, ..., Nc+1, where Nc = Trunc(Cu). When this modification is performed, the term $\frac{\partial c}{\partial x}(0,t)$ is introduced into the equation.

The *altered* ELLAM – which neglects $\frac{\partial c}{\partial x}(0,t)$ – employed in test cases 17a, 18a and 19a differs from the "unaltered" ELLAM in that it uses the unmodified equation 3.22 for all test functions $w_i^{n+1}(x,t)$; that is, no changes are performed on the equations when i = 0, 1, ..., Nc+1. For these test functions, one or more of the characteristic lines intersects the inflow boundary and "lands" *outside* the domain at points x_{i-1}^*, x_i^* and x_{i+1}^*, $t = t^n$. Furthermore, c(x,t) is *assumed* constant along characteristic lines outside of the domain (in reality this occurs only when D = 0 and K = 0) and so $c(x_{i-1}^*,t^n)$, $c(x_i^*,t^n)$, $c(x_{i+1}^*,t^n)$ are assumed equal to $c(0,t_{i-1}^*)$, $c(0,t_i^*)$, $c(0,t_{i+1}^*)$, respectively. The points $(0,t_{i-1}^*)$, $(0,t_i^*)$, $(0,t_{i+1}^*)$, where $t_k^* = t^{n+1} - k\,\frac{\Delta x}{V}$ (k is a dummy index) indicate the

location where the characteristic lines intersect the inflow boundary. The terms $c(0,t^*_{i-1})$, $c(0,t^*_i)$ and $c(0,t^*_{i+1})$ are approximated using linear interpolations, since $c(0,t^n)$ and $c(0,t^{n+1})$ are known in a Dirichlet problem. Once these values are calculated, they are assigned to $c(x^*_{i-1},t^n)$, $c(x^*_i,t^n)$, $c(x^*_{i+1},t^n)$, respectively, and the unmodified equation 3.22 is applied.

Results (figures 4.17, 4.18, 4.19) show that the ELLAM performs substantially better that the altered ELLAM, which neglects the term $\frac{\partial c}{\partial x}(0,t)$ and resembles traditional Eulerian–Lagrangian methods (ELM's).

Cases 20 and 21 are similar to tests 12 and 14, respectively. In the former two, a second (Neumann) type boundary condition is imposed at $x = 0$, the inflow spatial boundary. Error measurements for corresponding cases (i.e. 20 and 12, 21 and 14) are essentially the same, indicating that the ELLAM has the capability to produce excellent results for both Dirichlet and Neumann boundary conditions.

Figure 4.7: Results of test case 7 ($t^f = 0.25$). Solid curves indicate analytical solution values; dashed lines corresponds to the ELLAM numerical solution.

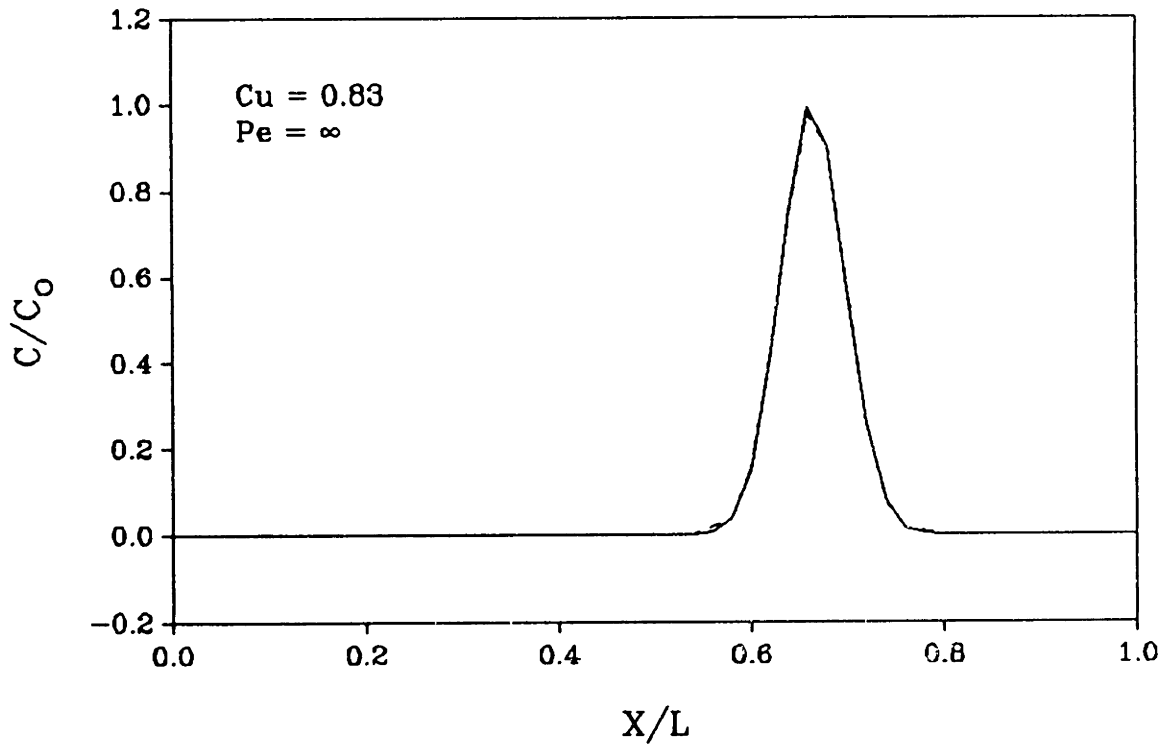

L2 Error Norm	ε	Ψ	μ_0
0.008542	0.014212	−0.000016	1.000000

Figure 4.8: Results of test case 8 ($t^f = 0.25$). Solid curves indicate analytical solution values; dashed lines corresponds to the ELLAM numerical solution.

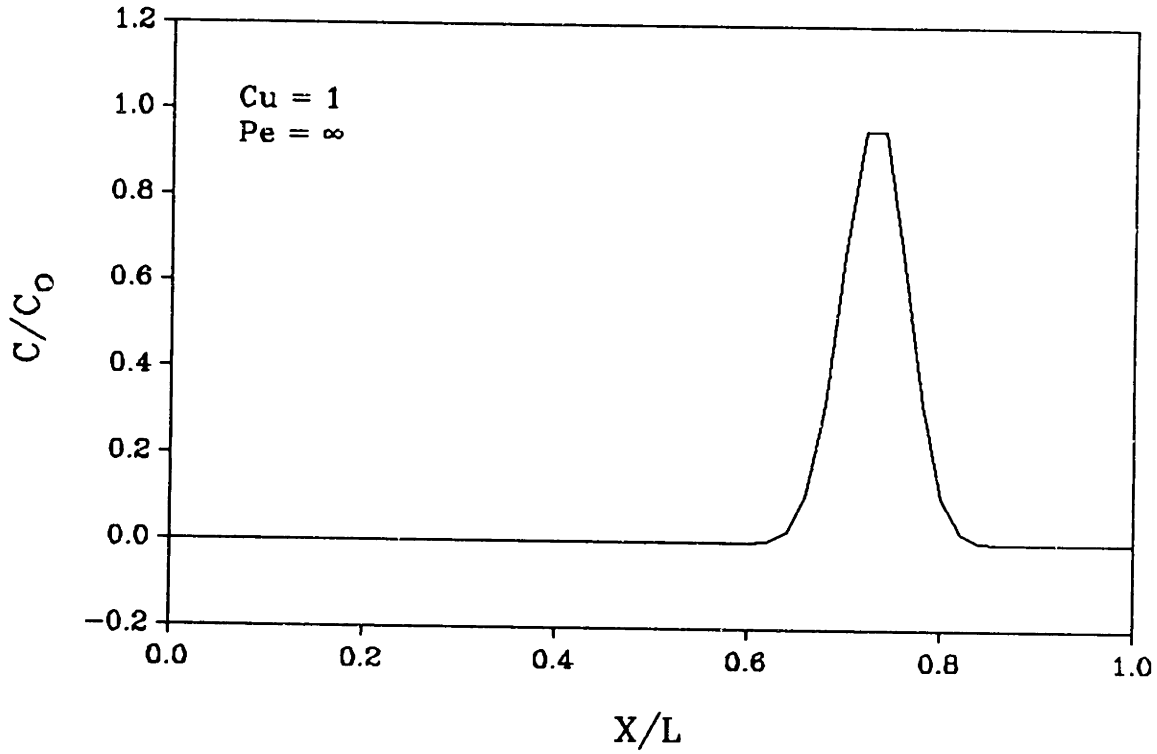

L2 Error Norm	ε	ψ	μ_0
0.006793	0.000000	0.000000	1.000000

Figure 4.9: Results of test case 9 ($t^f = 0.02$). Solid curves indicate analytical solution values; dashed lines corresponds to the ELLAM numerical solution.

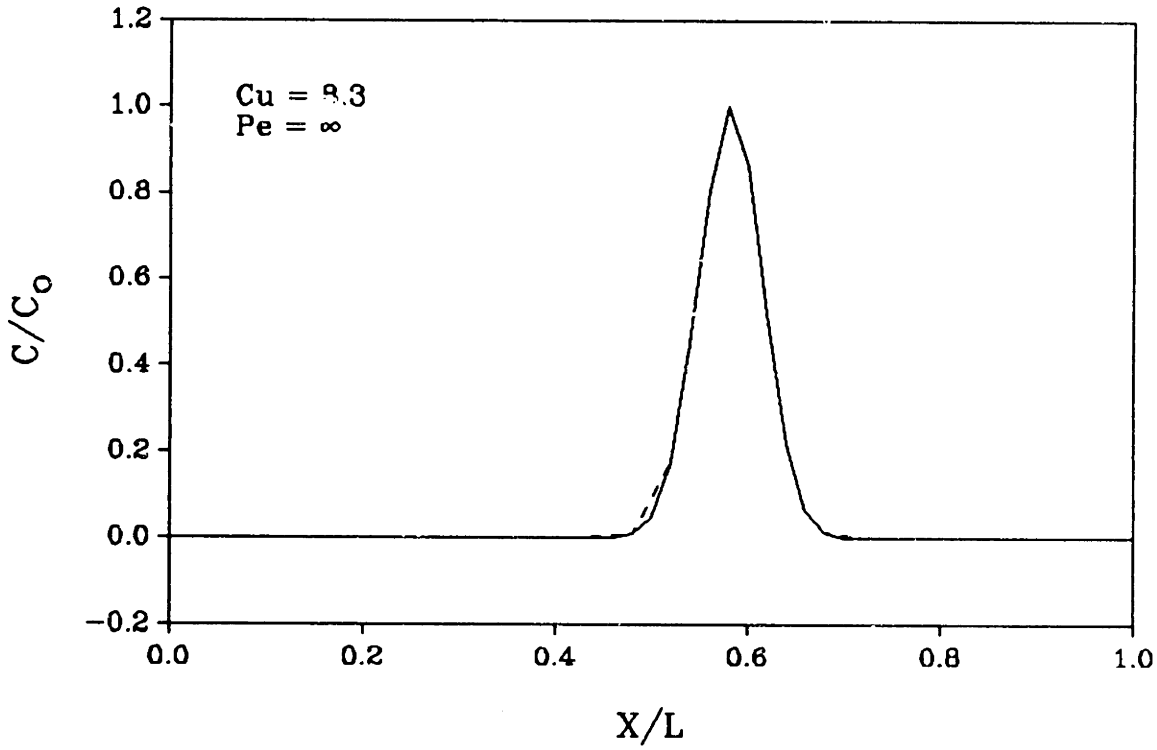

L2 Error Norm	ε	Ψ	μ_0
0.007060	0.001996	0.000000	1.000000

Figure 4.10: Results of test case 19 ($t^f = 0.02$). Solid curves indicate analytical solution values; dashed lines corresponds to the ELLAM numerical solution.

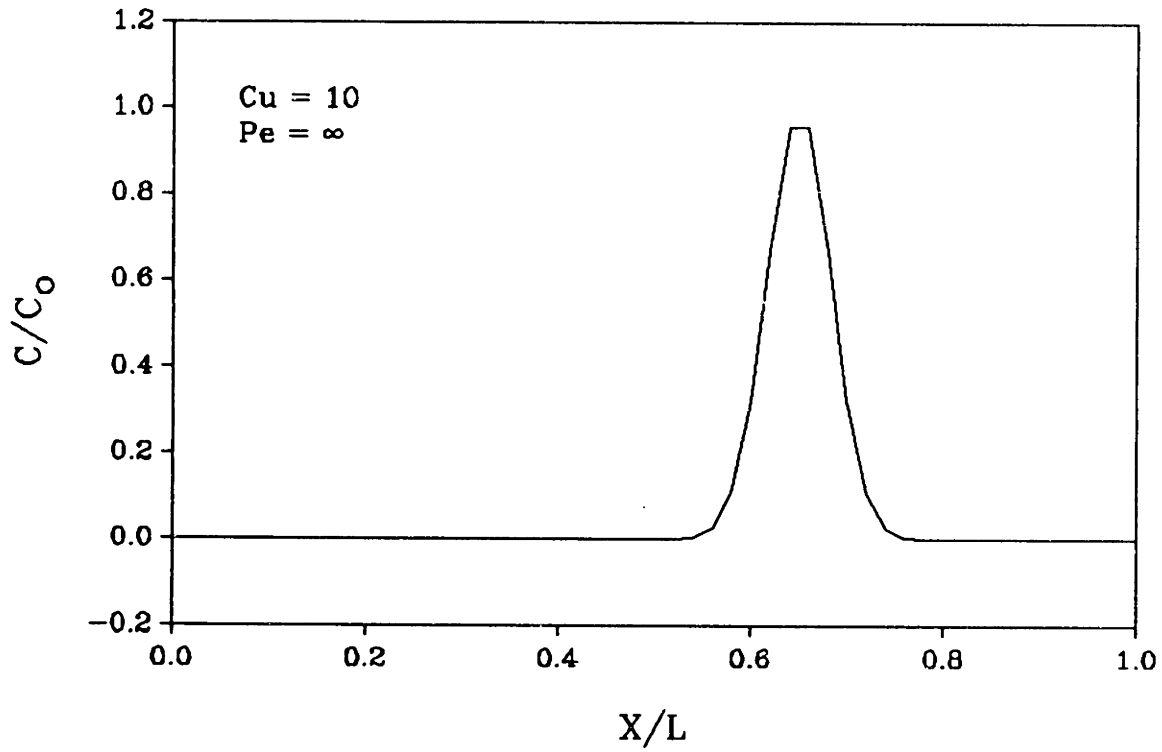

L2 Error Norm	ε	ψ	μ_o
0.006793	0.000000	0.000000	1.000000

Figure 4.11: Results of test case 11 ($t^f = 0.25$). Solid curves indicate analytical solution values; dashed lines corresponds to the ELLAM numerical solution.

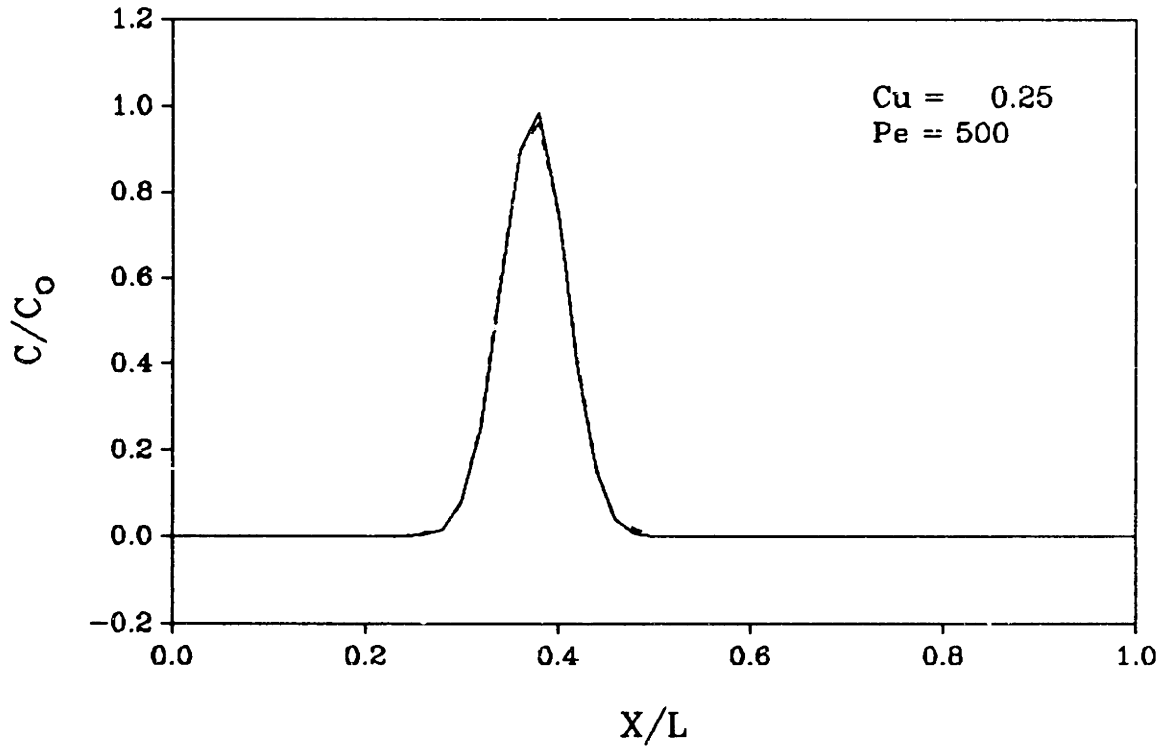

L2 Error Norm	ε	ψ	μ_0
0.009640	0.020809	-0.000064	1.000000

Figure 4.12: Results of test case 12 ($t^f = 0.25$). Solid curves indicate analytical solution values; dashed lines corresponds to the ELLAM numerical solution.

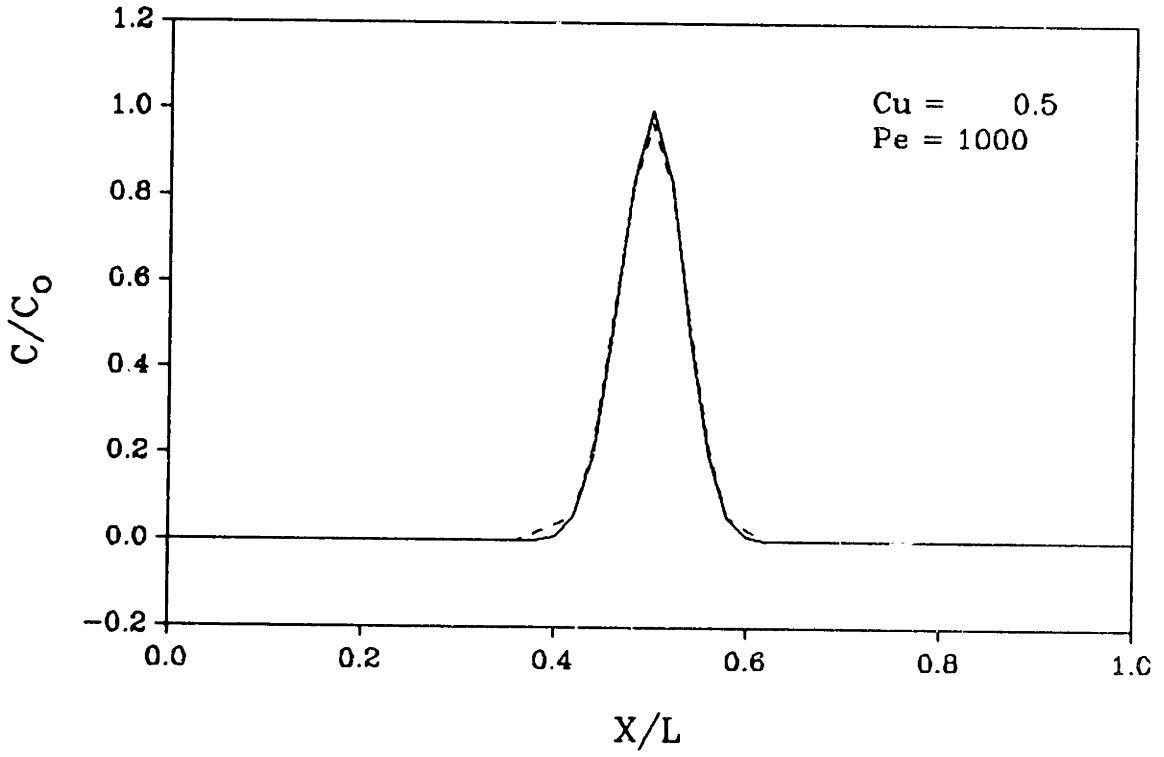

L2 Error Norm	ξ	ψ	μ_0
0.011549	0.029863	-0.000029	1.000000

Figure 4.13: Results of test case 13 ($t^f = 0.25$). Solid curves indicate analytical solution values; dashed iines corresponds to the ELLAM numerical solution.

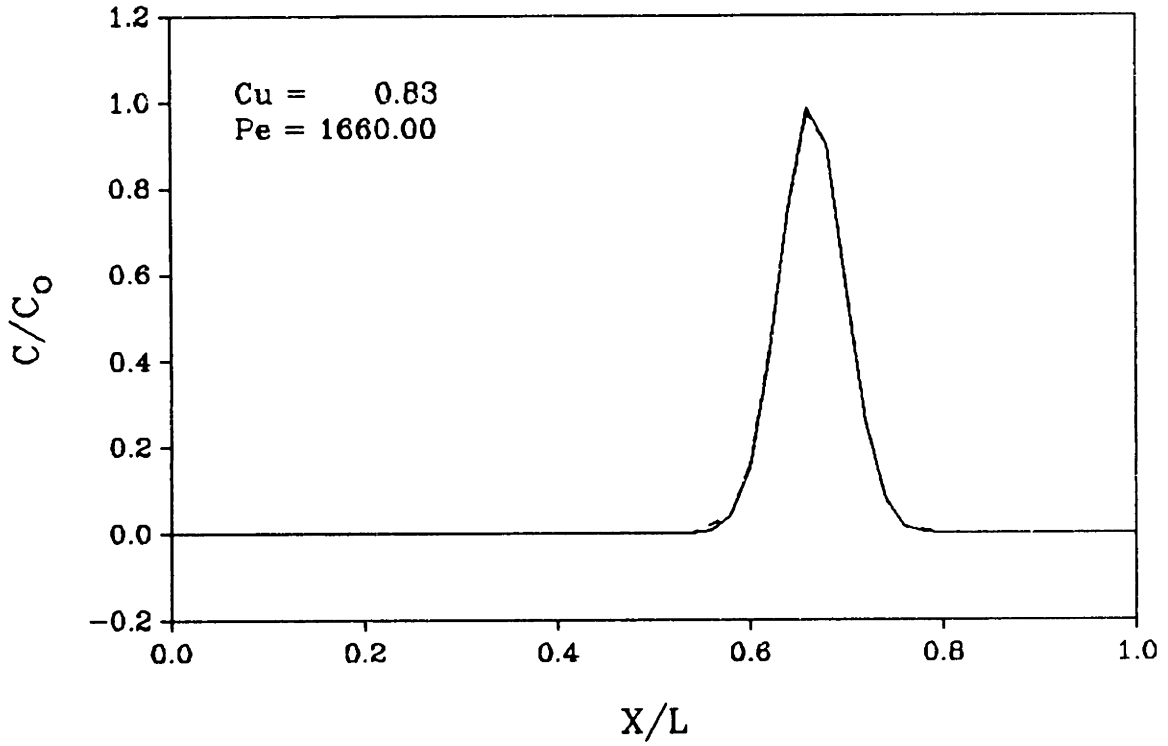

L2 Error Norm	ε	Ψ	μ_0
0.008459	0.014088	-0.000015	1.000000

Figure 4.14: Results of test case 14 ($t^f = 0.25$). Solid curves indicate analytical solution values; dashed lines corresponds to the ELLAM numerical solution.

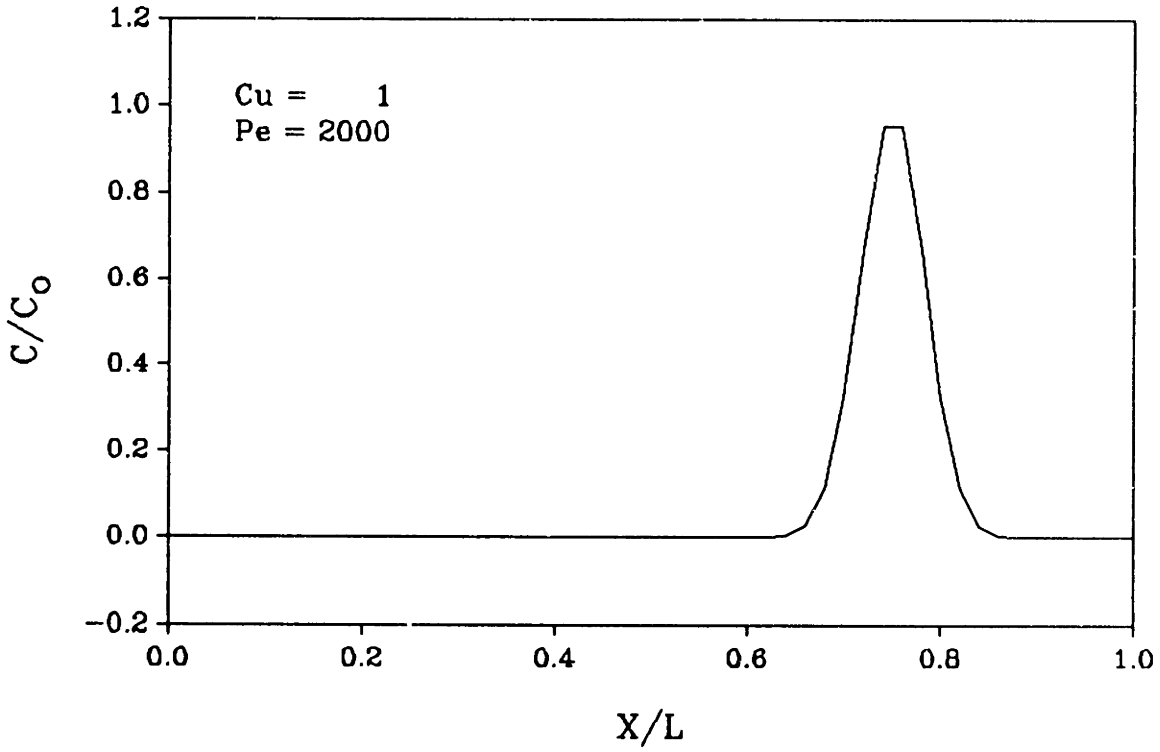

L2 Error Norm	ε	ψ	μ_0
0.006775	0.000339	0.000000	1.000000

Figure 4.15: Results of test case 15 ($t^f = 0.02$). Solid curves indicate analytical solution values; dashed lines corresponds to the ELLAM numerical solution.

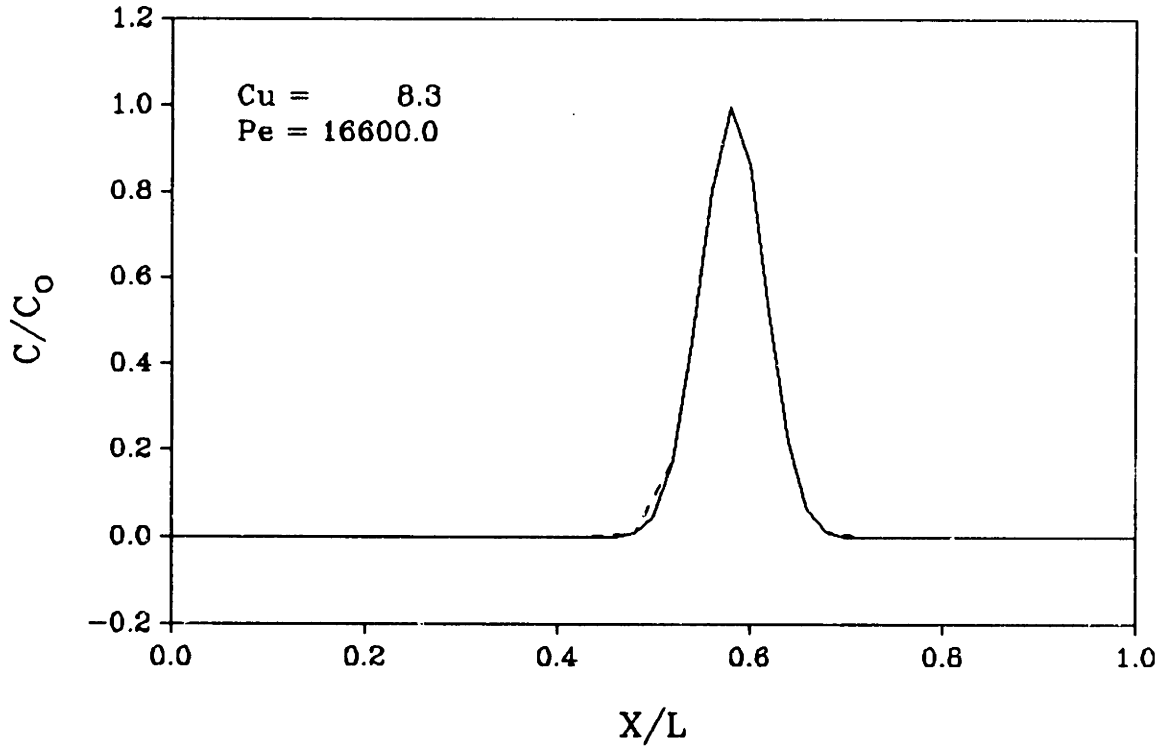

L2 Error Norm	ε	Ψ	μ_0
0.007055	0.002005	0.000000	1.000000

Figure 4.16: Results of test case 16 ($t^f = 0.02$). Solid curves indicate analytical solution values; dashed lines corresponds to the ELLAM numerical solution.

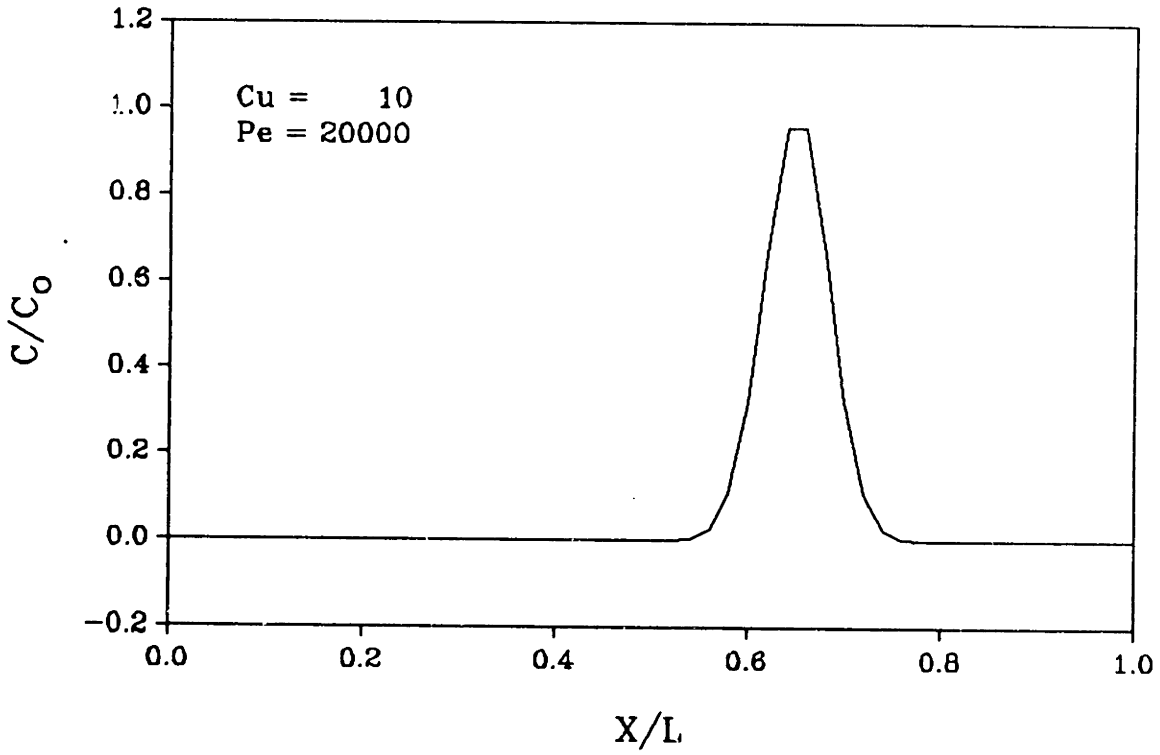

L2 Error Norm	ε	ψ	μ_o
0.006792	0.000027	0.000000	1.000000

Figure 4.16a : Solid curves indicate the initial condition used in tests 17a,b, 18a,b and 19a,b, where the location of the center of mass of the Gauss hill, x_o, is set to -0.25. Dotted curves show a concentration profile after crossing the inflow boundary.

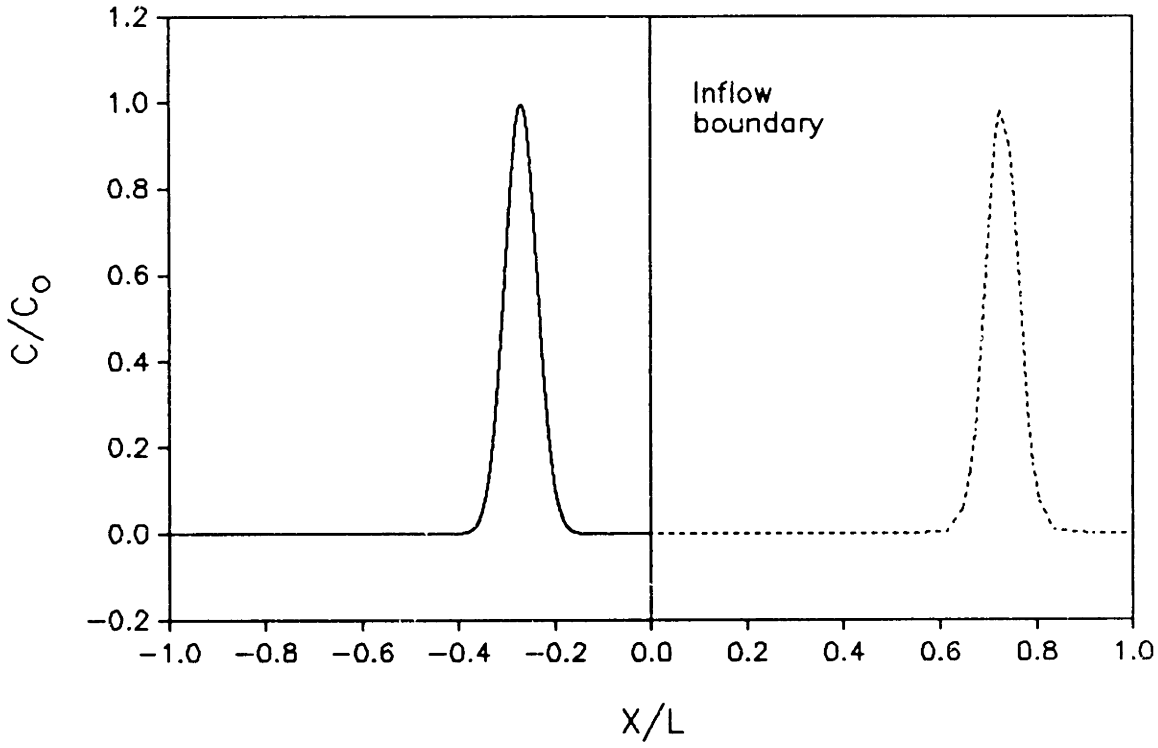

Figure 4.17: Results of test cases 17a and 17b ($t^f = 0.15$). (A) Concentration profile after crossing the inflow boundary obtained using an *altered* ELLAM formulation that resembles traditional ELM's; see text for explanation. (B) Concentration profile after crossing the inflow boundary obtained using the "unaltered" ELLAM numerical procedure. Solid curves indicate analytical solution values.

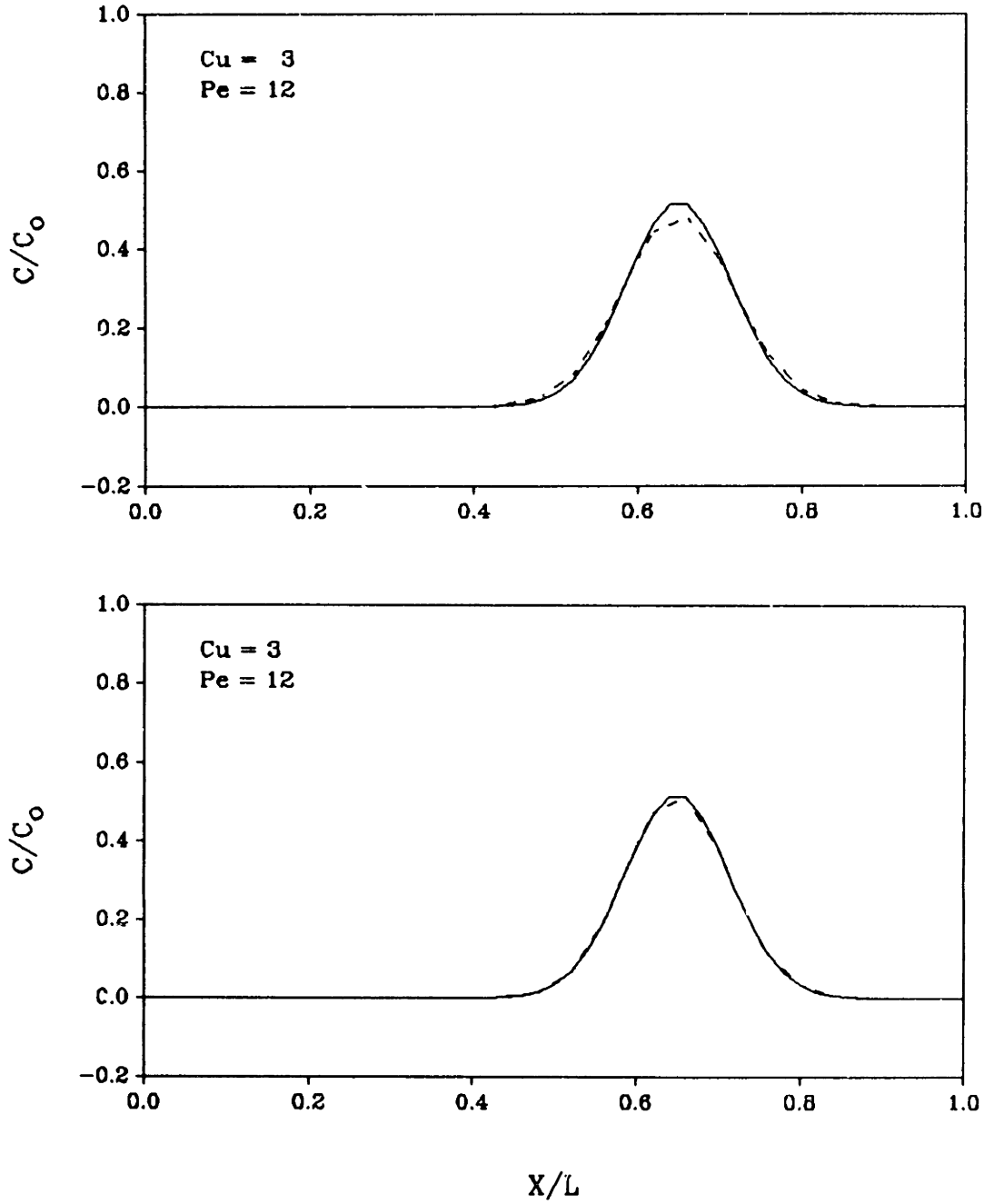

Test	L2 Error Norm	ε	Ψ	μ_0
17a	0.010781	0.061421	0.000000	0.999972
17b	0.001265	-0.005120	-0.000007	0.999960

Figure 4.18: Results of test cases 18a and 18b ($t^f = 0.15$). (A) Concentration profile after crossing the inflow boundary obtained using an *altered* ELLAM formulation that resembles traditional ELM's; see text for explanation. (B) Concentration profile after crossing the inflow boundary obtained using the "unaltered" ELLAM numerical procedure. Solid curves indicate analytical solution values.

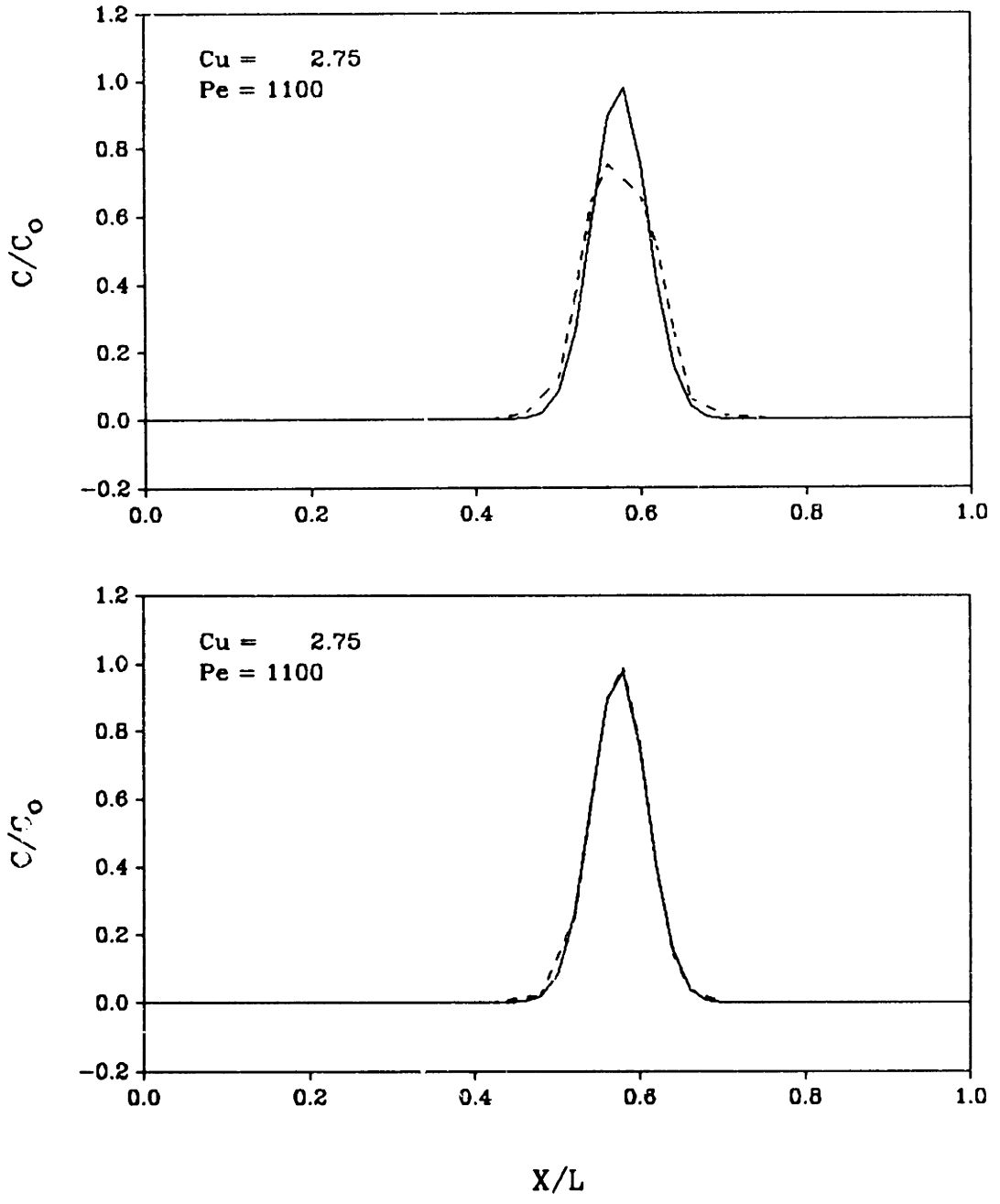

Test	L2 Error Norm	ε	ψ	μ_0
18a	0.052911	0.231589	–0.004421	0.998687
18b	0.005204	–0.015427	–0.000071	1.000408

Figure 4.19: Results of test cases 19a and 19b ($t^f = 0.15$). (A) Concentration profile after crossing the inflow boundary obtained using an *altered* ELLAM that resembles traditional ELM's; see text for explanation. (B) Concentration profile after crossing the inflow boundary obtained using the "unaltered" ELLAM numerical procedure. Solid curves indicate analytical solution values.

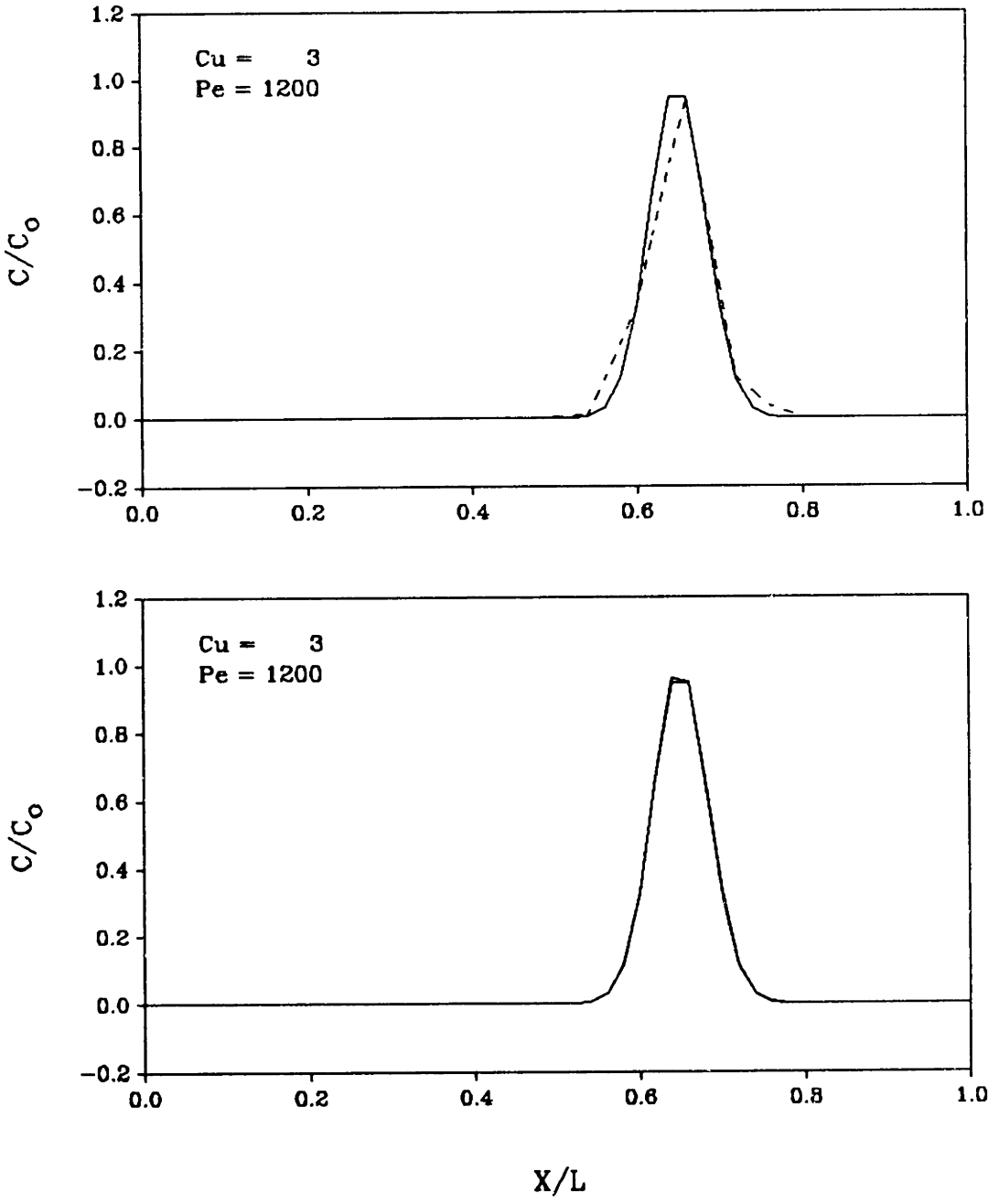

Test	L2 Error Norm	ε	Ψ	μ_0
19a	0.041000	0.014066	-0.000058	1.002253
19b	0.005391	-0.015320	-0.000001	1.000249

Figure 4.20: Results of test case 20 ($t^f = 0.25$), in which a second–type (Neumann) boundary condition is imposed at the inflow boundary. The same problem with a first–type (Dirichlet) boundary condition corresponds to test case 12. Solid curves indicate analytical solution values; dashed lines corresponds to the ELLAM numerical solution.

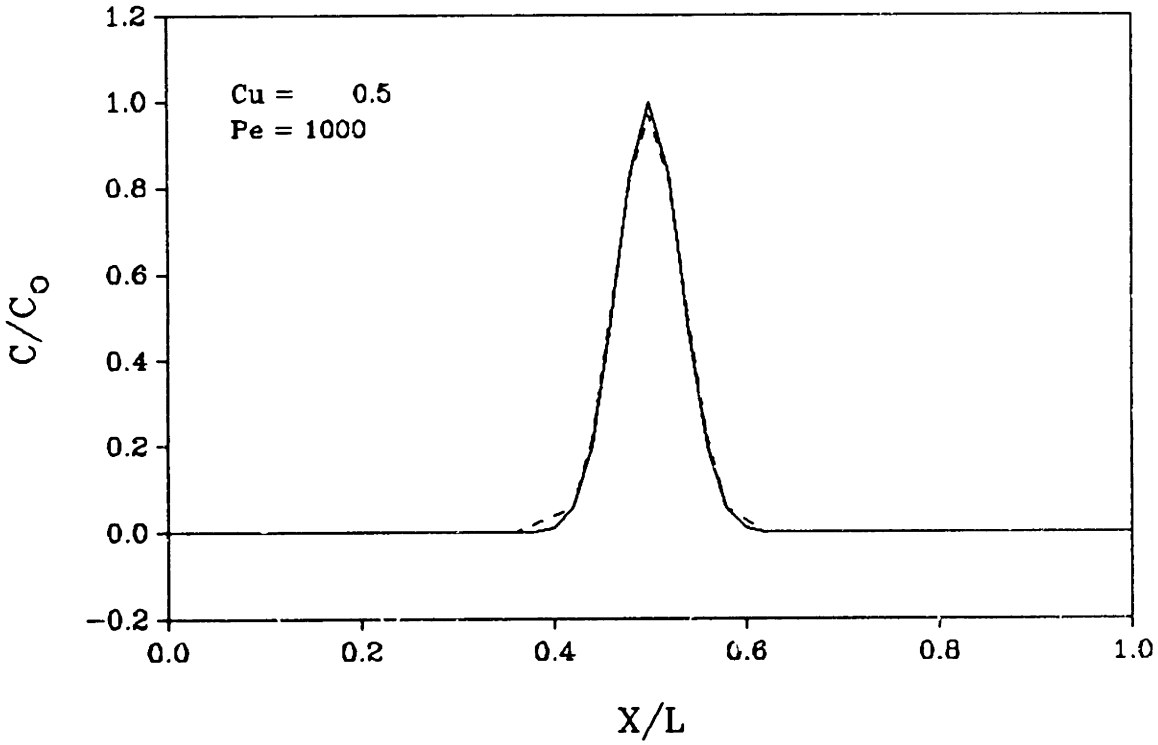

L2 Error Norm	ε	ψ	μ_0
0.011549	0.029863	–0.000029	1.000000

Figure 4.21: Results of test case 21 ($t^f = 0.25$), in which a second–type (Neumann) boundary condition is imposed at the inflow boundary. The same problem with a first–type (Dirichlet) boundary condition corresponds to test case 14. Solid curves indicate analytical solution values; dashed lines corresponds to the ELLAM numerical solution.

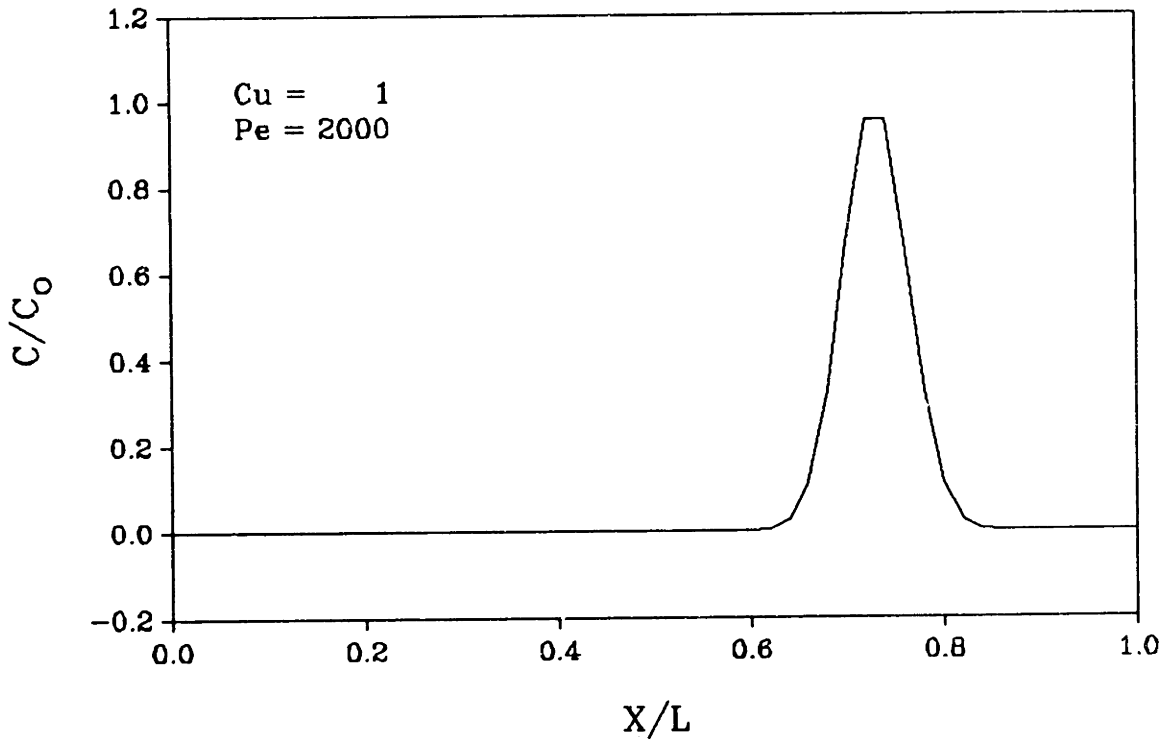

L2 Error Norm	ε	Ψ	μ_0
0.006776	0.000325	0.000000	1.000000

4.4 Advective–Diffusive–Reactive propagation of a Step Front

In this test, equation (4.1) – with non–zero R and K – is solved with initial condition

$$c(x,t) = 0 \quad 0 < x < l, \quad t = 0 \tag{4.9}$$

and boundary conditions

$$c(0,t) = 1, \quad t > 0, \tag{4.10a}$$

$$c(l,t) = 0, \quad t > 0, \text{ where } l \to \infty \tag{4.10b}.$$

The analytical solution is

$$c(x,t) = \frac{1}{2}\exp(\eta/2)\Big[\exp(\eta\sqrt{\alpha})\,\mathrm{erfc}\left(\sqrt{\alpha\tau} + \frac{\eta}{2\sqrt{\tau}}\right) + \exp(-\eta\sqrt{\alpha})\,\mathrm{erfc}\left(\frac{\eta}{2\sqrt{\tau}} - \sqrt{\alpha\tau}\right)\Big]$$

where

$$\eta = \frac{Vx}{D}, \quad \alpha = \left(\frac{1}{4} + K\frac{D}{V^2}\right), \quad \tau = \frac{V^2 t}{D}$$

For this problem, 6 test cases are considered; that is, cases 22 through 27. Each of these cases uses $\Delta x = 0.02$, $\Delta t = 0.1$, $Pe = 20$ (D is such that $Pe = 20$, $Pe \equiv \frac{V\Delta x}{D}$), and time weighting parameter $\theta = 0.5$. Initial and boundary conditions are as specified above.

Examples 22, 23, 26, and 27 (see figures 4.22 and 4.23), which use small Courant numbers ($Cu \leq 1$), show that the ELLAM performs very well for cases of reactive transport, although – just like in the first test problem (the propagation

of an initial step discontinuity) – the numerical results tend to be slightly ahead of the analytical solutions (for an explanation, see paragraph 4.2).

For large Courant numbers (e.g. 8.3 and 10, which are used in test cases 24 and 25, respectively) the ELLAM numerical solutions exhibit small non–physical oscillations as the front is approached from the upstream side (see figures 4.24 and 4.25). This particular behavior is due to the presence of the reaction term. Results for tests 3 and 6, for example, which deal with non–reactive (K = 0) transport, agree very well with analytical solutions, even though the Courant number increases from 1 in the former to 10 in the latter.

Figure 4.22: Results of test cases 22 and 26 ($t^f = 0.40$). Solid and dotted curves indicate analytical solution values; symbols corresponds to the ELLAM numerical solution: circles indicate results of case 22; diamonds designate results of case 26. Biodegradation uses R = 1 and K = 0.166 in equation (4.1); biodegradation and sorption employs R = 2 and K = 0.166.

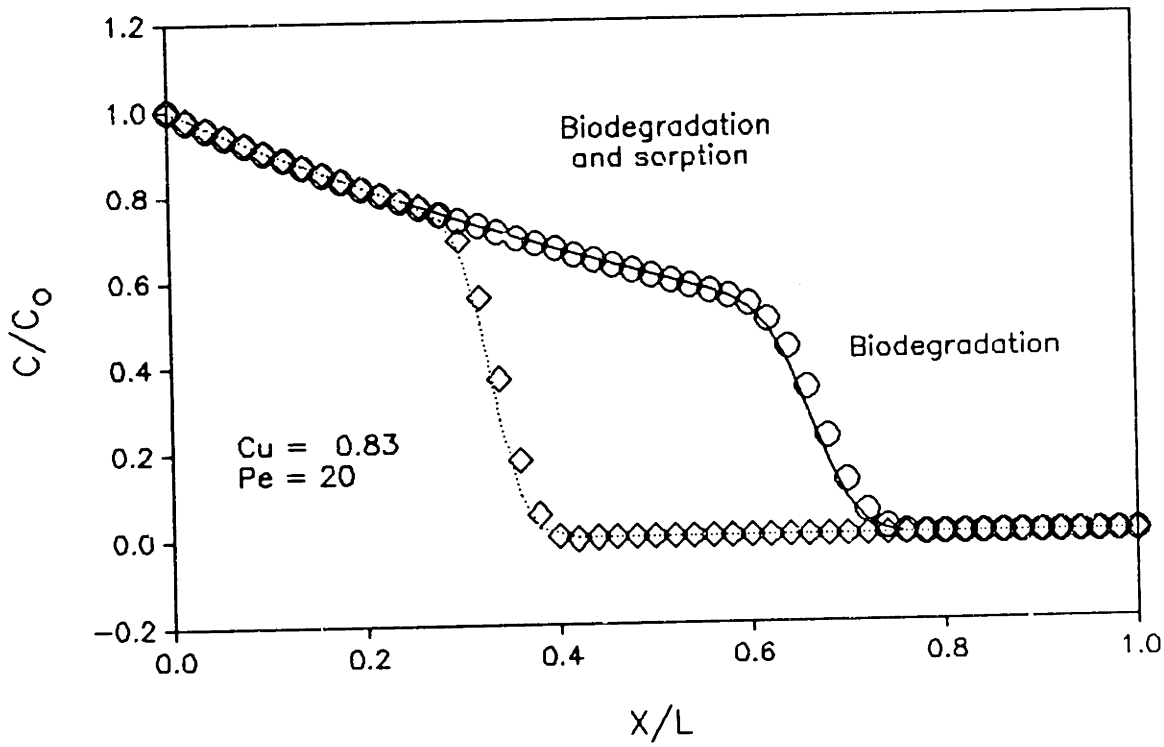

Test	L2 Error Norm	ξ	ψ	μ_0
22	0.013567	0.000000	0.000000	1.006760
26	0.020411	0.000000	−0.003676	1.020515

Figure 4.23: Results of test cases 23 and 27 ($t^f = 0.40$). Solid and dotted curves indicate analytical solution values; symbols corresponds to the ELLAM numerical solution: circles indicate results of case 23; diamonds designate results of case 27. Biodegradation uses R = 1 and K = 0.2 in equation (4.1); biodegradation and sorption employs R = 2 and K = 0.2.

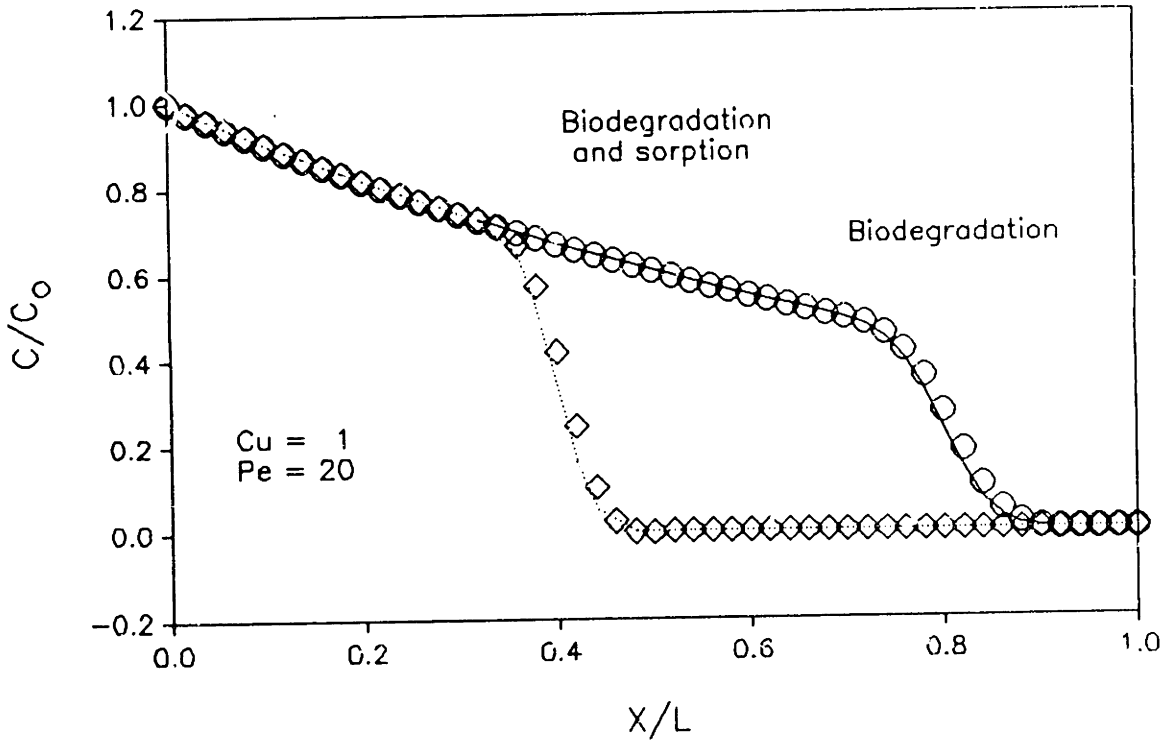

Test	L2 Error Norm	ε	λ	μ_0
23	0.011623	0.000000	−0.000025	1.003300
27	0.018691	0.000000	−0.001544	1.016364

Figure 4.24: Results of test case 24 ($t^f = 0.40$). Solid curves indicate analytical solution values; dashed lines corresponds to the ELLAM numerical solution.

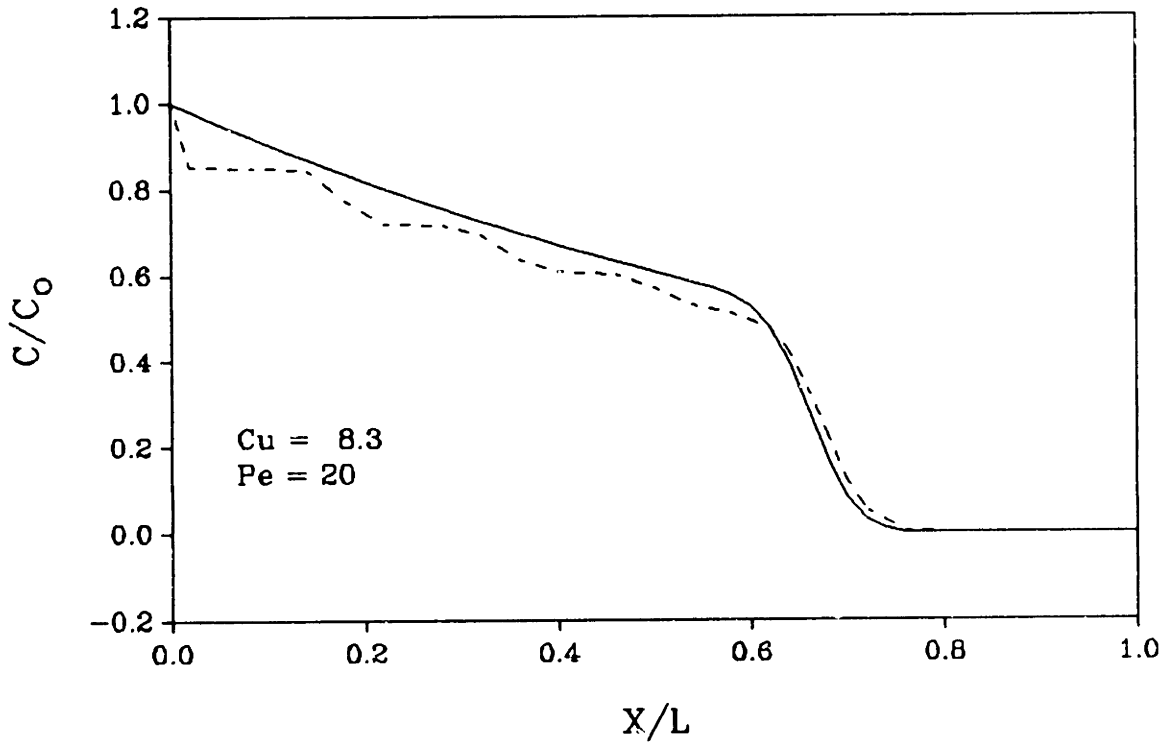

L2 Error Norm	ε	ψ	μ_0
0.048078	0.000000	0.000000	0.939445

Figure 4.25: Results of test case 25 ($t^f = 0.40$). Solid curves indicate analytical solution values; dashed lines corresponds to the ELLAM numerical solution.

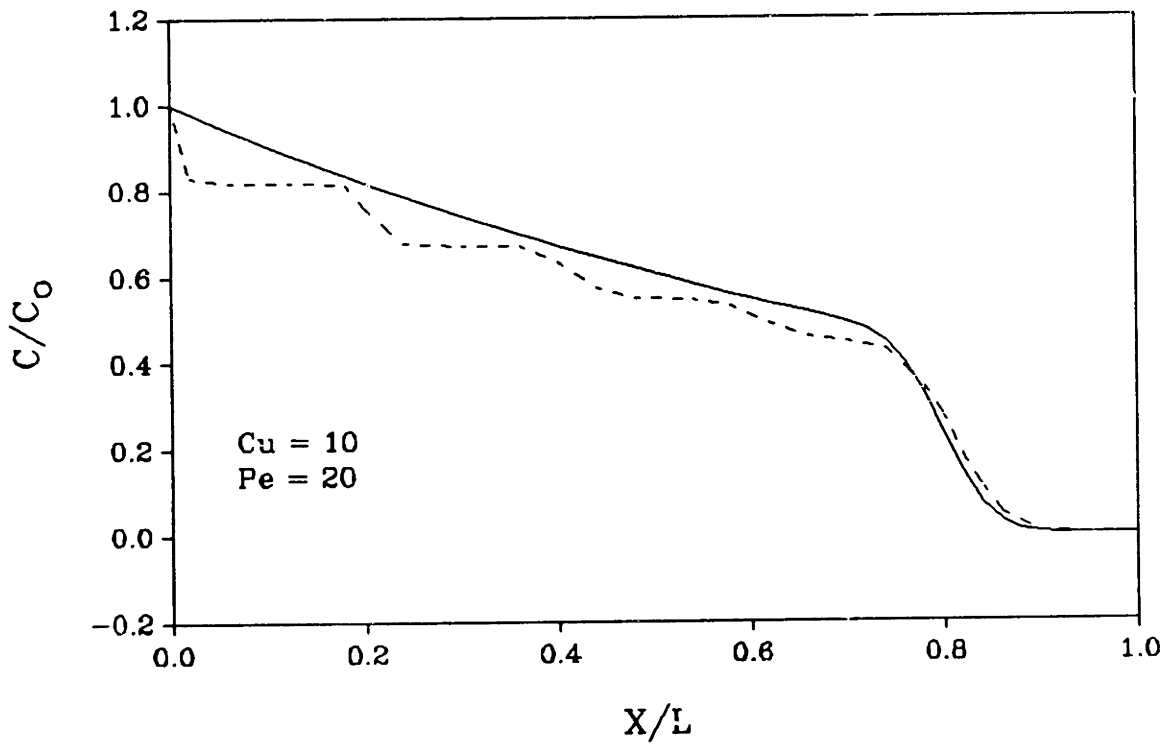

L2 Error Norm	ϵ	ψ	μ_0
0.060408	0.000000	0.000000	0.921704

4.5 Summary

The Courant number has an effect on the predictive capabilities of the ELLAM. The effect is, in general, more noticeable when considering reactive transport. This effect consists, for the reactive case, of some deterioration in the numerical solutions in the form of small non–physical oscillations as one approaches the concentration front from the upstream side when large Courant numbers are used (compare, for example, tests 22 and 23 with 24 and 25, respectively).

For non–reactive transport, test cases 1 through 21 demonstrate that the best numerical solutions are obtained for integer Courant numbers. The reason for this is that for integer Courant numbers no interpolations are required at the "foot of the characteristics" points to determine c(x,t) (see paragraph 4.2 for a more detailed explanation). Furthermore, the ELLAM has the ability to produce exact nodal values whenever D = 0 and an integer Courant number is used (see tests 8 and 10).

Finally, results for cases 20 and 12, and 21 and 14, indicate that the ELLAM performs very well for both Dirichlet or Neumann boundary conditions.

Chapter 5: CONCLUSIONS

The Eulerian–Lagrangian localized adjoint method (ELLAM) is a numerical solution procedure recently developed by Celia and co–workers (1989c) for the one–dimensional transient advection–diffusion equation. This new space–time formulation, which involves careful choice of test functions in a weak form statement of the problem, leads to a numerical approximation that accounts for all types of boundary conditions and that possesses the conservative property. Consequently, the ELLAM overcomes the two principal shortcomings of existing Eulerian–Lagrangian methods.

In this work the ELLAM is extended and applied to the one–dimensional constant–coefficient transient advective–diffusive–reactive equation. The extension involves the modification of test functions to reflect the influence of the reaction term. The resulting single formulation handles any combination of reaction, advection, and diffusion, including the case of zero diffusion.

Several example calculations are presented to demonstrate the behavior of the method. For the case of pure advection the ELLAM produces exact nodal values for the unknown function whenever integer Courant numbers are used. In this manner the method exhibits some optimality properties in the sense of the Optimal Test Function (OTF) formulation of Celia et al (1989b).

When advective–diffusive problems are considered, the ELLAM provides excellent results for a wide range of grid Peclet numbers, and thus is not restricted to only advection–dominated or diffusion–dominated systems. Moreover, the ELLAM appears to be considerably more accurate for simulation of advection–dominated systems than previously developed numerical schemes.

This is because the boundary conditions are treated in a systematic and rigorous way, which in turn leads to a mass conserving Eulerian–Lagrangian algorithm.

Results for reactive transport, on the contrary, exhibit small non–physical oscillations as the front is approached from the upstream side when large Courant numbers are used. The causes of this particular behavior remains to be explored, although it is likely due to the reaction term imposing limits time step size. Other areas of future research include the use of non–constant coefficients in the governing equation. For example, when the velocity is variable, the characteristics are, in general, not parallel. Hence, the space–time elements will no longer have straight edges, and accurate backtracking along characteristics becomes an important matter. The extension to multiple spatial dimensions is perhaps the most important step that remains. These issues should be addressed by combining the previous developments of classical Eulerian–Lagrangian methods with the new formulations of ELLAM.

REFERENCES

[1] Baptista, A. M., E. E. Adams, and K. D. Stolzenbach, "Eulerian–Lagrangian Analysis of Pollutant Transport in Shallow Water", Ralph M. Parsons Laboratory Report No. 296, MIT, (1984).

[2] Brooks, A. and T. J .R. Hughes, "Streamline upwind Petrov–Galerkin formulations of convection dominated flows with particular emphasis on the incompressible Navier–Stokes equations", *Comp. Meth. Appl. Mech. Engrg.*, 32, 199–259, (1982).

[3] Becker, E. B., G. F. Carey, and J. T. Oden, *Finite Elements: An Introduction*, Volume I, The Texas Finite Element Series, Prentice–Hall, Englewood Cliffs, N. J., (1981).

[4] Celia, M. A., I. Herrera, E. T. Bouloutas, and J. S. Kindred, "A new numerical approach for the advective–diffusive transport equation", *Num. Methods Partial Differential equations*, (1989a).

[5] Celia, M. A., J. S. Kindred and I. Herrera, "Contaminant transport and biodegradation 1. Numerical model for reactive transport in porous media", *Water Resources Research*, 25, 1141–1148, (1989b).

[6] Celia, M. A., T. Rusell, I. Herrera and R. Ewing, "An Eulerian–Lagrangian localized adjoint method for the advection–diffusion equation", (in preparation), (1989c).

[7] Freeze, R. A. and J. A. Cherry, *Groundwater*, Prentice–Hall, Englewood Cliffs, N. J., (1979).

[8] Heinrich, J. C., P. S. Huyakorn, O. C. Zienkiewicz, and A. R. Mitchell, "An 'up–wind' finite element scheme for two–dimensional convective–transport equation", *Int. J. Num. Meth. Engrg.*, 11, 131–143, (1977).

[9] Hughes, T. J. R., "A simple scheme for developing 'upwind' finite elements", *Int. J. Num. Meth. Engrg.*, 15, 1939–1365, (1978).

[10] Huyakorn, P. S., "Upwind finite element scheme for improved solution of the convection–diffusion equation", Water Resources Program Report 76–WR–7, Princeton University, (1976).

[11] Javandel, I., C. Doughty. C. F. Tsang, *Groundwater Transport: Handbook of Mathematical Models*, Water Resources Monograph Series 10, Americal Geophysical Union, Washington, D.C., (1984).

[12] Lapidus, L. and G. F. Pinder, *Numerical Solution of Partial Differential Equations in Science and Engineering*, John Wiley, (1982).

[13] Neuman, S. P., "An Eulerian–Lagrangian numerical scheme for the dispersion–convection equation using conjugate space–time grids", *J. Comp. Phys.*, 41(2), 270–294, (1981).

[14] Neuman, S. P., "Adaptive Eulerian–Lagrangian finite element method for advection–dispersion", *Int. J. Num. Meth. Engrg.*, 20, 321–337, (1984).

[15] Neuman, S. P and S. Sorek, "Eulerian–Lagrangian methods for advection–dispersion", *in Finite Elements in Water Resources*, Proc. Fourth Intern. Conf. in Hannover, Germany (K. P. Holz, U. Meissner, W. Zielke, C. A. Brebbia, G. F. Pinder and W. G. Gray, Eds), Berlin, 14.41–14.68, (1982).

[16] Pinder, G. F. and W. G. Gray, *Finite element simulation in surface and subsurface hydrology*, Academic Press, New York, (1977).

[17] U.S. Environmental Protection Agency, *Waste Disposal Practices and Their Effects on Ground Water: The Report to Congress*, Washington, D.C., (1977).

[18] Van der Heijde, P., Y. Bachmat, J. Bredehoeft, B Andrews, D. Holtz, S. Sebastian, *Groundwater Management: the use of numerical models*, Water Resources Monograph 5, American Geophysical Union, Washington, D.C., (1985).

[19] Van Genuchten, M. Th. and W. G. Gray, "Analysis of some dispersion corrected numerical schemes for solution of the transport equation", *Int. J. Num. Meth. Engrg.*, 12, 387–404, (1978).

[20] Varoğlu, E. and W. D. L. Finn, "Finite elements incorporating characteristics for one–dimensional diffusion–convection equation", *J. Comp. Phys.*, 34, 371–389, (1980).